

Anomalous Hydrogen Recombination-Line Ratios in Ultraluminous Infrared Galaxies

KENICHI YANO,^{1,2} SHUNSUKE BABA ^{3,*} TAKAO NAKAGAWA ² MATTHEW MALKAN,⁴ NAOKI ISOBE,² MAI SHIRAHATA,²
RYOSUKE DOI,^{1,2} AND VANSHREE BHALOTIA ⁵

¹*Department of Physics, Graduate School of Science, The University of Tokyo, 7-3-1 Hongo, Bunkyo-ku, Tokyo 113-0033, Japan*

²*Institute of Space and Astronautical Science, Japan Aerospace Exploration Agency, 3-1-1 Yoshinodai, Chuo-ku, Sagami-hara, Kanagawa 252-5210, Japan*

³*National Astronomical Observatory of Japan, 2-21-1 Osawa, Mitaka, Tokyo 181-8588, Japan*

⁴*Department of Physics and Astronomy, University of California, Los Angeles, CA 90095-1547, USA*

⁵*Department of Physics and Astronomy, University of Hawai'i at Mānoa, 2505 Correa Rd, Honolulu, HI 96822, USA*

(Received Dec 25, 2020; Revised Aug 16, 2021; Accepted Sep 13, 2021)

Submitted to ApJ

ABSTRACT

We conducted systematic observations of the H I Br α (4.05 μ m) and Br β (2.63 μ m) lines in 52 nearby ($z < 0.3$) ultraluminous infrared galaxies (ULIRGs) with *AKARI*. Among 33 ULIRGs wherein the lines are detected, three galaxies show anomalous Br β /Br α line ratios (~ 1.0), which are significantly higher than those for case B (0.565). Our observations also show that ULIRGs have a tendency to exhibit higher Br β /Br α line ratios than those observed in Galactic H II regions. The high Br β /Br α line ratios cannot be explained by a combination of dust extinction and case B since dust extinction reduces the ratio. We explore possible causes for the high Br β /Br α line ratios and show that the observed ratios can be explained by a combination of an optically thick Br α line and an optically thin Br β line. We simulated the H II regions in ULIRGs with the Cloudy code, and our results show that the high Br β /Br α line ratios can be explained by high-density conditions, wherein the Br α line becomes optically thick. To achieve a column density large enough to make the Br α line optically thick within a single H II region, the gas density must be as high as $n \sim 10^8$ cm⁻³. We therefore propose an ensemble of H II regions, in each of which the Br α line is optically thick, to explain the high Br β /Br α line ratio.

Keywords: Active galaxies — Starburst galaxies — Ultraluminous infrared galaxies

1. INTRODUCTION

Ultraluminous infrared galaxies (ULIRGs) are characterized by their enormous infrared luminosities L_{IR} (8–1000 μ m), which exceed $10^{12}L_{\odot}$ (Sanders et al. 1988). Large infrared luminosity is produced by thermal radiation from heated dust. This indicates that powerful energy sources are hidden behind dust. Since the discovery of ULIRGs in the 1980s, it has been debated whether the dominant energy source in a ULIRG is due to starburst activity and/or to an active galactic nucleus (AGN) (e.g., Sanders et al. 1988; Sanders & Mirabel

1996). However, the large amount of dust harbored in a ULIRG makes it difficult to investigate the energy source observationally, and thus it is important to determine the amount of dust extinction in a ULIRG in order to correct the observed quantities.

One of the most widely used indicators of dust extinction is the ratio of hydrogen recombination lines. These lines have been extensively studied and are widely used as tracers of ionized gas because hydrogen is the simplest and most abundant element in the universe (e.g., Seaton 1959; Johnson 1972; Hummer & Storey 1987; Storey & Hummer 1995). The ratio of the H I line fluxes from photoionized gas can be calculated numerically for the so-called the “case B” model, in which all the Lyman-line photons are assumed to be absorbed by other hydrogen atoms, and all other H I lines are assumed to be optically thin. The line ratios calculated for case B

Corresponding author: Shunsuke Baba
shunsuke.baba@nao.ac.jp

* JSPS Fellow (PD)

are widely recognized to explain the observed line ratios in Galactic H II regions and in nearby starburst galaxies (e.g., [Osterbrock & Ferland 2006](#)). Comparing the observed line ratios with those from case B enables us to determine the amount of dust extinction in the H I lines. In optical-through-infrared wavelengths, the dust extinction is larger at shorter wavelengths (e.g., [Draine 2003](#)). Thus, if we determine the ratio of two H I lines, the line with the shorter wavelength is affected more by extinction than the one with the longer wavelength, and hence the observed line ratio deviates from the case B prediction. Accordingly, we can evaluate dust extinction using the deviation of the observed line ratio from the case B value.

The H I line ratio that is most widely used to determine dust extinction is the ratio of the optical H α and H β lines (e.g., [Veilleux et al. 1995](#); [Kim et al. 1998](#)), i.e., the so-called Balmer decrement, because the wavelengths of these lines are easily accessible from ground-based telescopes. However, in objects such as ULIRGs, which are heavily dust-obscured, the dust extinction is so high that the optical Balmer lines trace only the outer regions of the object and therefore underestimate the extinction. To avoid this problem, we focus here on the infrared H I lines Br α ($\mathcal{N} = 5 \rightarrow 4$, 4.051 μm) and Br β ($\mathcal{N} = 6 \rightarrow 4$, 2.626 μm), which are less affected by dust extinction compared with the optical lines. For instance, the H β /H α line ratio is nearly halved from the case B result by dust extinction of $A_V \sim 1$ mag, whereas the Br β /Br α line ratio is reduced by only $\sim 4\%$ from case B by the same extinction ([Draine 2003](#)). In contrast, dust extinction of $A_V > 15$ mag is expected in ULIRGs (e.g., [Genzel et al. 1998](#)); the Br β /Br α line ratio is half that of case B with this large dust extinction. Thus, the Br β /Br α line ratio is expected to be a good indicator of high dust extinction in ULIRGs.

To investigate the Br α and Br β lines simultaneously, we utilized near-infrared spectroscopy from the *AKARI* infrared satellite ([Murakami et al. 2007](#); [Onaka et al. 2007](#)). Owing to its unique 2.5–5.0 μm wavelength coverage, which is not completely achievable with ground-based telescopes due to Earth’s atmosphere, we can determine the Br β /Br α line ratio without observational bias such as aperture differences. In this study, we discuss the results of systematic observations of the Br β /Br α line ratios in ULIRGs from *AKARI* and report the discovery of an anomaly in the H I line ratio, which we cannot explain with case B and dust extinction. We also present the results of narrow-band imaging observations of the H α line flux using the Nickel 40-inch telescope at Lick Observatory, which we compare with the *AKARI* results. In Section 2, we present

our targets, observations, and methods of data reduction. The resulting spectra and measured fluxes of the Br α , Br β , and H α lines are presented in Section 3. The observed Br β /Br α line ratios are compared with those for case B, and we conclude that some ULIRGs show an anomalously high Br β /Br α line ratio. This cannot be explained by a combination of dust extinction and case B since dust extinction reduces the ratio. In Section 4, we discuss possible causes of the high Br β /Br α line ratio. We find that the anomaly can be explained with high-density H II regions which make the Br α line optically thick. This high-density model is compared with other observations of H I lines in Section 5. Possible structures of high-density H II region in ULIRGs are discussed in Section 6. We present some implications from our results in Section 7 and summarize our study in Section 8. Throughout this paper, we assume that the universe is flat, with $\Omega_M = 0.27$, $\Omega_\Lambda = 0.73$, and $H_0 = 70.4 \text{ km s}^{-1} \text{ Mpc}^{-1}$ ([Komatsu et al. 2011](#)). We also assume the Milky Way dust model of [Draine \(2003\)](#) for the extinction curve. In that model, dust extinction at the wavelengths of the H α , H β , Br α , and Br β lines are taken to be $A_{H\alpha} = 0.776A_V$, $A_{H\beta} = 1.17A_V$, $A_{Br\alpha} = 3.56 \times 10^{-2}A_V$, and $A_{Br\beta} = 8.19 \times 10^{-2}A_V$, respectively.

2. OBSERVATIONS AND DATA REDUCTION

First, we describe our *AKARI* observations; targets and methods of data reduction. Then, we present details of our *Nickel* observations.

2.1. *AKARI*

2.1.1. *Targets*

Among the pointed observations from *AKARI*, we focused on those conducted during the liquid-He-cooled holding period (2006 May 8 to 2007 August 26; [Murakami et al. 2007](#)) to obtain high-quality data. Among those observations, we further focused on data obtained by the mission program “Evolution of ultraluminous infrared galaxies and active galactic nuclei” (AGNUL: P.I., T. Nakagawa). This is the same dataset as that used by [Yano et al. \(2016\)](#). The AGNUL program conducted systematic near-infrared spectroscopic observations of ULIRGs in the local universe. During the liquid-He-cooled holding period, 50 near-infrared grism spectroscopic observations of ULIRGs were conducted in this program. The observation log and basic information, such as redshifts and infrared luminosities of the 50 AGNUL targets, are summarized in Tables 1 and 2 of [Yano et al. \(2016\)](#), respectively.

In addition, we visually inspected all near-infrared spectra obtained with the InfraRed Camera (IRC) dur-

ing the liquid-He-cooled holding period against the “IRC Point Source Spectral Catalogue.”¹ We searched for possible targets to be included in the present study and found two galaxies (IRAS 09022–3615 and IRAS 10565+2448) in which the Br α and Br β lines were clearly detected. They were observed by the mission program “The nature of new ULIRGs at intermediate redshift” (NULIZ: P.I., H. HoSeong). To enlarge the sample size, we added these two targets to our sample. The observation log and basic information for the two objects are summarized in Appendix A. Altogether, we analyzed the near-infrared spectroscopic data for 52 objects using the observations described above.

2.1.2. Reduction of Spectroscopic Data

The near-infrared spectroscopic observations we analyzed were obtained with the IRC spectrograph (Onaka et al. 2007) on board the *AKARI* infrared satellite (Murakami et al. 2007). We used a 1×1 arcmin² window to avoid source overlap. The pixel scale of the *AKARI* IRC was $1''.46 \times 1''.46$. We used the NG grism mode (Onaka et al. 2007) to obtain a 2.5–5.0 μm spectrum. The NG grism has a dispersion of $9.7 \times 10^{-3} \mu\text{m pix}^{-1}$ and an effective spectral resolution of $\lambda/\delta\lambda \sim 120$ at 3.6 μm for a point source. We employed the observing mode IRC04, in which one pointing comprised eight or nine independent frames. Thus, although we assigned only one pointing for each ULIRG, we were able to eliminate the effects of cosmic-ray hits. The total net on-source exposure time was ~ 6 min for each ULIRG.

We processed the data using “IRC Spectroscopy Toolkit Version 20181203,” the standard IDL toolkit prepared for the reduction of *AKARI* IRC spectra (Ohyama et al. 2007; Baba et al. 2016). The process was basically the same as that used by Yano et al. (2016) but we used the latest version of the toolkit. Each frame was dark-subtracted, linearity-corrected, and flat-field corrected. Wavelength and flux calibrations were also made within the toolkit, but once a spectrum was output, we manually adjusted the wavelength calibration based on the location of the Br α line (§3.1). We take the accuracy of the final wavelength calibration to be smaller than 0.2 pixel or $\sim 2 \times 10^{-3} \mu\text{m}$.

The latest version of the tool kit, which we used in the current study, incorporates an error propagation algorithm that we have revised. In older versions, the flux error in the output spectrum contained the sum of the three components: (1) error determined from the

standard deviation of the blank sky signal, (2) error due to the uncertainty of the spectral response curve, and (3) error caused by the wavelength calibration uncertainty. Component (1) is statistical error and should be included in the measurement of line fluxes and their ratios. Component (2) has two factors: (2a) uncertainty of scaling independent of wavelength, and (2b) uncertainty of curve shape change depending on wavelength. Of these, (2a) affects the measurement of line fluxes as a systematic error, and is canceled out in the calculation of line-to-line ratios. On the other hand, (2b) remains even in the line ratio estimate and should be included. For component (3), the toolkit conservatively considers the accuracy of the wavelength origin to be 1 pixel or $\sim 0.01 \mu\text{m}$ by default (Ohyama et al. 2007). In this work, since we have tuned the origin as mentioned above, component (3) is actually negligible. Thus, since the purpose of this paper is the Br β /Br α line ratio, components (1) and 2(b) should be included in the error budget, while 2(a) and (3) are not. The latest version of the toolkit has been revised so that components (1), (2), and (3) can be output separately, so (3) can be excluded. However, it is difficult to disentangle sub-components (2a) and (2b). Therefore, we have included components (1) and (2) (=2a) and (2b)) in our analysis as a conservative estimate for the Br β /Br α ratio.

We estimated the spatial extension of an object by stacking the spectrum along the dispersion direction for each source. The measured FWHM of the spatial profile is typically ~ 4 –5 pixels, which is consistent with the size of the point-spread function of the *AKARI* IRC in the spectroscopic mode (Lorente et al. 2008). We adopted an aperture width of 5 pixels (= $7''.3$) along the spatial direction for spectrum extraction for each ULIRG.

We analyzed the spectroscopic data for 52 objects, as described in §2.1.1. Since the eastern (E) and western (W) nuclei of IRAS 17028+5817 are resolved by the *AKARI* IRC, the spectra of the two nuclei were extracted separately. Thus, 53 spectra in total were obtained from the 52 observations. Figure 1 displays a sample 2.5–5.0 μm spectrum of a ULIRG.

2.2. Nickel 40-inch Telescope

For two selected targets, IRAS 10494+4424 and Mrk 273, which we find to show the anomalous Br β /Br α ratio (§3.3), we performed narrow-band imaging observations of the H α line ($\mathcal{N} = 3 \rightarrow 2$, 6563 Å) with the Nickel 40-inch telescope at the Lick Observatory. In order to compare the H α line flux with the Brackett-line fluxes obtained from the *AKARI* observations, aperture matching becomes important. Our *AKARI* observations employed slitless spectroscopy, and we used

¹ The catalog is publicly available at URL: http://www.ir.isas.jaxa.jp/AKARI/Observation/update/20160425_preliminary_release.html

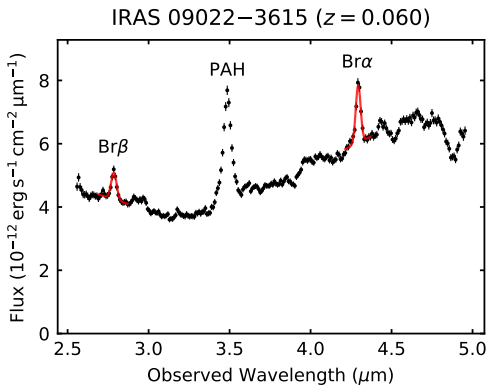


Figure 1. Example of an *AKARI* IRC 2.5–5.0 μm spectrum of a ULIRG. The best-fit Gaussian profiles for the Br α and Br β lines are plotted in red.

an aperture width of $\sim 7''$ to extract the near-infrared spectra. We used the narrow-band imaging observations to obtain the H α line fluxes with the same aperture as adopted for *AKARI*.

We performed the Lick observations on 2014 November 26. We used the same observational method as described in Theios et al. (2016). The sky was clear, with seeing of $\sim 2''$ FWHM. We used the Nickel Direct Imaging Camera (CCD-C2), which has 2048×2048 pixels, which we read out with 2×2 binning to yield 1024×1024 pixels $0''.37$ on a side. The observed wavelength of the H α line was 7167 \AA at the redshift of IRAS 10494+4424 ($z = 0.092$) and 6811 \AA at that of Mrk 273 ($z = 0.037$). The filters (central wavelength/FWHM in \AA) that we used to measure the flux of the H α line were $7146/80$ for IRAS 10494+4424 and $6826/78$ for Mrk 273 (on-band images). We used the 6826 filter for IRAS 10494+4424 and the 7146 filter for Mrk 273 to measure the flux of the underlying continuum (off-band images). We obtained three exposures in each of the H α and continuum filters, with individual exposure times of 900 s. We dithered the telescope between exposures to mitigate the effects of hot or bad pixels in the detector. We also obtained bias and twilight-sky flat-field frames for each filter.

We reduced the data using standard IRAF procedures, including bias and flat-field corrections. We averaged the three dithered frames in each filter and subtracted the off-band from the on-band images to obtain a pure H α + [N II] line image. The narrow-band filters were photometrically calibrated by observing standard stars and comparing them with data from the Sloan Digital Sky Survey (Ahn et al. 2012). The fluxes through the filters were consistent with each other to within 5%.

3. RESULTS

3.1. Fluxes of Brackett Lines

We obtained 2.5–5.0 μm near-infrared spectra for 53 objects with *AKARI*, as discussed in the previous section. For each spectrum, the Br α line, at a rest-frame wavelength of $\lambda_{\text{rest}} = 4.05 \mu\text{m}$, and the Br β line, at $\lambda_{\text{rest}} = 2.63 \mu\text{m}$, were fitted separately with a linear continuum and a Gaussian profile.

First, we fitted the Br α line with four free parameters: the offset and slope of the linear continuum, the normalization of the Gaussian profile, and the central wavelength. The line width was fixed at the spatial width at wavelengths near Br α (FWHM ~ 4 –5 pixels) since *AKARI* IRC employs slitless spectroscopy and the instrumental line spread function is determined by the spatial point spread function. We assumed that the spectral resolution was determined by the size of each object because the observations employ slitless spectroscopy and the intrinsic line widths are narrower than the Δv resolution of $\sim 3000 \text{ km s}^{-1}$. The range of wavelengths used to fit continuum emission was typically $\pm 0.08 \mu\text{m}$ around the central wavelength. The central wavelengths of the Br α lines exhibited small discrepancies from those expected from the redshifts. The discrepancy was larger than the fitting error, typically $\sim 10^{-3} \mu\text{m}$, but was within the wavelength calibration error of $\sim 10^{-2} \mu\text{m}$ (Ohya et al. 2007). Therefore, we shifted the wavelengths for the entire spectrum so that the best-fit central wavelength of the Br α line matched the redshift. Next, after fitting the Br α line, we fitted the Br β line, fixing the central wavelength as expected from the redshift and fixing the line width at the spatial width near the wavelength of Br β as in the case of Br α ; i.e., the free parameters are the offset and slope of the local continuum and the normalization of the Gaussian. We then determined the fluxes of the Br α and Br β lines by integrating the best-fit Gaussian profiles. We show a typical result from this Gaussian fitting procedure in Figure 1.

Among the 53 objects, we were able to determine the fluxes of the Br α and Br β lines for 47 galaxies. Four of the sources (IRAS 00183–7111, IRAS 04313–1649, IRAS 10091+4704, and IRAS 23498+2423) have redshifts higher than 0.2; therefore, the Br α line does not fall within the 2.5–5.0 μm wavelength range. In addition, two sources (IRAS 21477+0502 and IRAS 23129+2548) were found to suffer from spectral overlapping with other objects. In UGC 5101, we found the continuum slope to be changing in the vicinity of the Br β line; thus, we adopted a second-order polynomial for the shape of the continuum used to fit the Br β line for this source.

We detected the Br α or Br β lines at the 3σ level in 33 objects. For undetected lines, we derived 3σ upper-limit fluxes. The measured Br α and Br β line fluxes ($F_{\text{Br}\alpha}$ and

$F_{\text{Br}\beta}$) are summarized in Table 1, along with the 1σ statistical errors; the 1σ systematic errors were estimated to be $\sim 10\%$ of the flux.

Table 1. Fluxes of Brackett Lines

Object Name	$F_{\text{Br}\alpha}^a$ (10^{-15} erg s $^{-1}$ cm $^{-2}$)	$F_{\text{Br}\beta}$	$F_{\text{Br}\beta}/F_{\text{Br}\alpha}$	A_V^b (mag)
IRAS 00456–2904	6.80 \pm 0.69	2.73 \pm 0.83	0.40 \pm 0.13	8.0 \pm 7.5
IRAS 00482–2721	4.37 \pm 0.43	<2.72	<0.62	> –2.3
IRAS 01199–2307	2.90 \pm 0.80	<2.20	<0.76	> –6.9
IRAS 01298–0744	<1.86	<4.02
IRAS 01355–1814	<2.56	<2.40
IRAS 01494–1845	4.02 \pm 0.80	5.5 \pm 1.0	1.37 \pm 0.37	–20.7 \pm 6.4
IRAS 01569–2939	4.4 \pm 1.4	<4.97	<1.12	> –16
IRAS 02480–3745	<4.15	<2.48
IRAS 03209–0806	4.39 \pm 0.49	2.75 \pm 0.73	0.63 \pm 0.18	–2.4 \pm 6.8
IRAS 03521+0028	<3.63	<4.38
IRAS 04074–2801	<3.16	5.08 \pm 0.93	>1.61	< –24
IRAS 05020–2941	4.7 \pm 1.0	<3.32	<0.70	> –5.0
IRAS 05189–2524	<16.8	<17.1
IRAS 06035–7102	8.1 \pm 1.0	3.80 \pm 0.93	0.47 \pm 0.13	4.2 \pm 6.5
IRAS 08572+3915	25.3 \pm 2.5	<5.94	<0.23	> 21
IRAS 08591+5248	2.77 \pm 0.84	6.15 \pm 0.81	2.22 \pm 0.73	–32.0 \pm 7.7
IRAS 09022–3615	68.8 \pm 3.3	35.8 \pm 2.2	0.520 \pm 0.041	1.9 \pm 1.8
UGC 5101	18.4 \pm 2.9	<40.8	<2.21	> –32
IRAS 09463+8141	1.86 \pm 0.51	<2.54	<1.36	> –21
IRAS 09539+0857	<3.36	<2.13
IRAS 10035+2740	<1.90	<3.09
IRAS 10494+4424 ^C	10.92 \pm 0.83	10.5 \pm 1.1	0.96 \pm 0.12	–12.4 \pm 3.0
IRAS 10565+2448 ^C	35.2 \pm 2.1	31.1 \pm 2.4	0.883 \pm 0.085	–10.5 \pm 2.3
IRAS 10594+3818	8.4 \pm 1.4	5.51 \pm 0.93	0.66 \pm 0.16	–3.5 \pm 5.5
IRAS 11028+3130	<3.46	<3.36
IRAS 11180+1623	<4.44	<2.04
IRAS 11387+4116	4.86 \pm 0.89	<2.33	<0.48	> 3.9
IRAS 12447+3721	5.63 \pm 0.80	3.54 \pm 0.99	0.63 \pm 0.20	–2.5 \pm 7.4
Mrk 231	<73.1	<71.2
Mrk 273 ^C	49.4 \pm 1.1	53.7 \pm 2.3	1.086 \pm 0.053	–15.3 \pm 1.1
IRAS 13469+5833	<3.32	<4.66
IRAS 13539+2920	14.0 \pm 1.2	5.5 \pm 1.7	0.39 \pm 0.12	8.5 \pm 7.4
IRAS 14121–0126	4.1 \pm 1.2	<4.59	<1.12	> –16
IRAS 14202+2615	8.03 \pm 0.91	7.18 \pm 0.68	0.89 \pm 0.13	–10.8 \pm 3.5
IRAS 14394+5332	9.5 \pm 1.1	8.62 \pm 0.54	0.91 \pm 0.12	–11.2 \pm 3.0

Table 1 *continued*

Table 1 (*continued*)

Object Name	$F_{\text{Br}\alpha}^a$	$F_{\text{Br}\beta}$	$F_{\text{Br}\beta}/F_{\text{Br}\alpha}$	A_V^b
	$(10^{-15} \text{ erg s}^{-1} \text{ cm}^{-2})$			(mag)
IRAS 15043+5754	3.31 ± 0.87	3.6 ± 1.0	1.10 ± 0.42	-15.6 ± 8.9
IRAS 16333+4630	4.03 ± 0.99	< 3.19	< 0.79	> -7.9
IRAS 16468+5200	< 3.16	< 3.24
IRAS 16487+5447	10.19 ± 0.78	4.2 ± 1.2	0.41 ± 0.12	7.5 ± 7.1
IRAS 17028+5817 E	3.80 ± 0.69	< 4.88	< 1.28	> -19
IRAS 17028+5817 W	6.14 ± 0.91	5.5 ± 1.1	0.90 ± 0.23	-11.0 ± 6.0
IRAS 17044+6720	6.6 ± 1.1	< 3.95	< 0.60	> -1.3
IRAS 17068+4027	6.53 ± 0.90	3.40 ± 0.93	0.52 ± 0.16	1.9 ± 7.2
IRAS 17179+5444	< 3.45	< 4.59
IRAS 19254-7245	20.1 ± 1.6	13.8 ± 2.0	0.69 ± 0.11	-4.6 ± 3.8
IRAS 22088-1831	< 2.58	< 2.35
IRAS 23128-5919	67.0 ± 3.3	41.2 ± 2.7	0.614 ± 0.050	-2.0 ± 1.9

^aObserved flux of the Br α line. The values differ from those reported in Yano et al. (2016) because we used a different version of the toolkit for the data reduction and revised the error estimation as reported in this paper.

^bVisual extinction derived from the observed Br β /Br α line ratio assuming case B.

^cGalaxies showing clear anomalies in the Br β /Br α line ratio.

The widths of the Br α and Br β lines are consistent with the limit of spectral resolution ($\Delta v \sim 3000 \text{ km s}^{-1}$) for all targets within a fitting uncertainty of $\leq 100 \text{ km s}^{-1}$. This indicates that none of the objects shows a broad component of the Br lines with a FWHM broader than $\sim 1000 \text{ km s}^{-1}$. If the broad-line region of an AGN had contributed to the line fluxes, the hydrogen lines would have had a FWHM of a few thousand km s^{-1} (Osterbrock & Ferland 2006). Thus, we conclude that the Br α and Br β lines do not originate from the broad-line regions. In the AGNUL sample, Yano et al. (2016) reported a good correlation between the flux of the Br α line and the $3.3 \mu\text{m}$ polycyclic aromatic hydrocarbon (PAH) emission and suggested that any contribution from an AGN was not dominant for the Br α line. Combining these results, we conclude that the Brackett lines originate from starburst activities in all galaxies in the sample.

3.2. Flux of H α Line

We obtained pure H α + [N II] line images for IRAS 10494+4424 and Mrk 273 from the Nickel observations. Using the IRAF phot module, we performed circular-aperture photometry ($7''$ in diameter) for the images and obtained the H α + [N II] line fluxes. Assuming [N II]/H α line ratios to be 0.60 for IRAS 10494+4424 and 1.01 for Mrk 273 (Kim et al. 1998), we corrected the

Table 2. Observed H α Line Flux

Object	$F_{\text{H}\alpha}$
	$(10^{-14} \text{ erg s}^{-1} \text{ cm}^{-2})$
IRAS 10494+4424	1.46 ± 0.15
Mrk 273	33.1 ± 3.3

line ratios for the [N II] emission. The resulting H α line fluxes are summarized in Table 2. We discuss the H α line flux in comparison with the Br α line flux in §4.

3.3. Anomalous Br β /Br α Line Ratios

Owing to the unique 2.5–5.0 μm wavelength coverage of AKARI, the Br α and Br β lines are observed simultaneously within a single spectrum. This allows us to determine accurately the Br β /Br α line ratio without introducing observational uncertainties such as aperture corrections. The estimated Br β /Br α line ratios are summarized in Table 1. On the basis of the Br β /Br α line ratio, we were able to determine the visual extinction (A_V) in the same way as for the usual Balmer-decrement method. We assumed the intrinsic line-flux ratio for Br β /Br α to be 0.565 (Osterbrock & Ferland 2006, case B with $T = 10000 \text{ K}$ and low-density limit). If dust extinction affects the line fluxes, the Br β /Br α line ratio

decreases because the Br β line has a shorter wavelength and is attenuated more compared with the Br α line. Thus, we expect to observe Br β /Br α line ratios lower than 0.565. In Table 1, we also tabulate the values of A_V inferred from the Br β /Br α line ratio.

The comparison of $F_{\text{Br}\alpha}$ and $F_{\text{Br}\beta}$ is shown in Figure 2. Galaxies located below the case B line in Figure 2 have a Br β /Br α line ratio lower than 0.565. The flux ratios for these galaxies are consistent with case B theory and dust extinction, and the A_V magnitude was found to be positive for these objects. However, for four galaxies, we obtained an anomalous Br β /Br α line ratio, which is more than 3σ higher than 0.565. These galaxies are located above the case B line in Figure 2; i.e., the Br β line is enhanced relative to the Br α line. This is opposite to the effect of dust extinction.

We examined the spectra of the four galaxies that deviate by more than 3σ from case B in Figure 2; they are IRAS 04074–2801, IRAS 10494+4424, IRAS 10565+2448, and Mrk 273. Among them, IRAS 04074–2801 is relatively faint, and the continuum is considerably affected by a fringe-like pattern. We found that if the wavelength range for fitting the Br β line is widened by a factor of 1.5, the Br β line flux decreases by $\sim 20\%$ for this galaxy. Thus, we excluded IRAS 04074–2801 from our discussion of the high Br β /Br α line ratio because of the large uncertainties in determining the continuum underlying the line. For the remaining three galaxies for which the spectra are shown in Figure 3, a change in the wavelength range does not affect the line fluxes by more than 5%. We conclude that the three galaxies (shown as blue circles in Figure 2), IRAS 10494+4424, IRAS 10565+2448, and Mrk 273, show Br β /Br α line ratios of 0.96 ± 0.12 , 0.883 ± 0.085 , and 1.086 ± 0.053 , respectively, all significantly higher than the case B ratio (0.565). These line-ratio anomalies are not explainable with case B theory and dust extinction, which could reduce but not increase the Br β /Br α line ratio. We show the spectra around the Br α and Br β lines for these three galaxies in Figure 4.

We found no distinct physical properties to distinguish the three galaxies (IRAS 10494+4424, IRAS 10565+2448, and Mrk 273) with high Br β /Br α line ratios from the other sources. The optical classifications of these galaxies are LINER, H II galaxy, and Seyfert 2 (Veilleux et al. 1999a). The three galaxies have been observed at infrared wavelengths, as reported in several publications (e.g., Imanishi et al. 2008; Veilleux et al. 2009; Lee et al. 2012). Infrared properties, such as the strengths of their PAH emissions, were compared to those of other ULIRGs, but no significant differences were reported.

One common observational property is that the three objects have relatively low redshifts ($z \sim 0.09$ for IRAS 10494+4424 and $z \sim 0.04$ for IRAS 10565+2448 and Mrk 273) compared to the others in our sample; accordingly, the Br α and Br β lines are detected with a high S/N ratio, and the Br β /Br α line ratio is well-determined in the three galaxies. Thus, they provide clear detections of deviations of the Br β /Br α line ratio from case B. This implies that anomalous Br β /Br α line ratios might also exist in faint galaxies for which we have not been able to verify its presence because of large uncertainties in the observed Br β /Br α line ratios.

To investigate whether the anomaly is actually found in faint galaxies, we averaged the near-infrared spectra of 35 galaxies with $F_{\text{Br}\alpha} < 10^{-14}$ erg s $^{-1}$ cm $^{-2}$. Each spectrum was corrected for redshift and was averaged in rest wavelength. The averaged spectrum of the 35 galaxies is shown in Figure 5. We measured the values of $F_{\text{Br}\alpha}$ and $F_{\text{Br}\beta}$ from the averaged spectrum using Gaussian fitting, obtaining $F_{\text{Br}\alpha} = (3.21 \pm 0.20) \times 10^{-15}$ erg s $^{-1}$ cm $^{-2}$ and $F_{\text{Br}\beta} = (2.30 \pm 0.16) \times 10^{-15}$ erg s $^{-1}$ cm $^{-2}$. This yields a Br β /Br α line ratio of 0.716 ± 0.065 , which is 2.3σ higher than the case B value of 0.565. Although the significance of this result is not high enough ($< 3\sigma$), it is opposite to the expectation that ULIRGs should show high dust extinction; i.e., the Br β /Br α line ratio should be lower than 0.565. We thus conclude that in future high-sensitivity observations, such as those with the *James Webb Space Telescope* (JWST), anomalous Br β /Br α line ratios may be found in faint galaxies for which we have not been able to determine the presence of the anomaly with current AKARI observations.

3.4. Estimate of Contamination of Brackett Lines

One possible cause of the line-ratio anomaly is that the Brackett lines may be blended with other features. The spectral resolution of our observations is not high ($\sim 0.04\text{--}0.05$ μm); therefore, the apparently high Br β /Br α line ratio may be caused by contamination due to other features. We looked for such features, with wavelengths close to those of the Brackett lines. However, there are few observations around the wavelengths of the Brackett lines (especially around the Br β line) because the wavelength is difficult to access from the ground due to atmospheric absorption. Little information is therefore available about possible contaminant features.

We reviewed a list of infrared atomic lines provided by ISO observations (Table 4.10 of Glass 1999) and found no candidate lines near the wavelengths of the Br β and Br α lines. Among molecular features (Table 4.10 of Cox

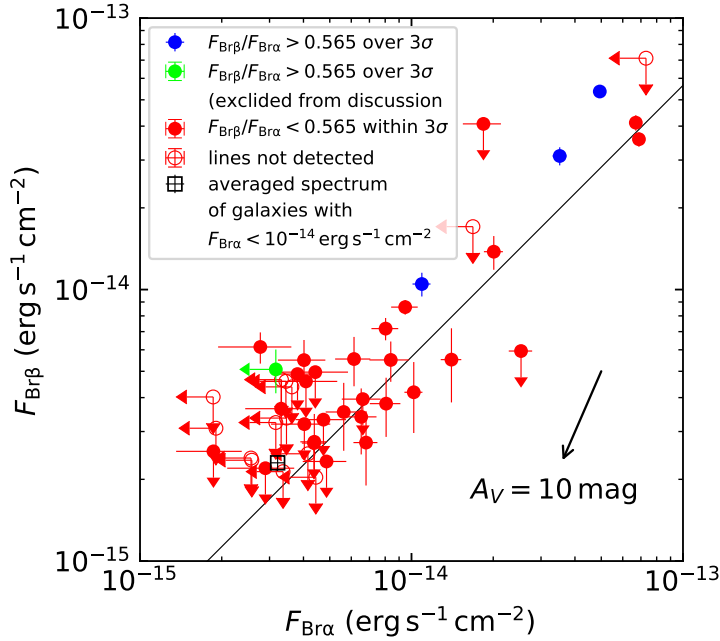


Figure 2. The Br α line flux ($F_{\text{Br}\alpha}$) versus the Br β line flux ($F_{\text{Br}\beta}$). The solid line shows the theoretical line ratio for case B conditions: $F_{\text{Br}\beta}/F_{\text{Br}\alpha} = 0.565$. The extinction vector for $A_V = 10$ mag is shown as a black arrow. The blue filled circles show galaxies with anomalous Br β /Br α line ratios (more than 3σ higher than 0.565), while red filled circles represent those with the normal case B ratio. The green filled circles show galaxies with high Br β /Br α line ratios but they have been excluded from the discussion because of large uncertainties in determining the continuum underlying the lines. The red open circles represent galaxies where neither the Br α nor Br β lines were detected. The black open square shows the averaged spectrum of 35 galaxies with $F_{\text{Br}\alpha} < 10^{-14}$ erg s $^{-1}$ cm $^{-2}$.

2000), we found one candidate line, H $_2$ (1,0) O(2), for which the wavelength is 2.627 μm . The wavelength of this line is very close to that of the Br β line; therefore, the flux of the Br β line could be overestimated due to contamination by the molecular hydrogen line. We discuss below the possible effect of molecular hydrogen contamination on the Br β /Br α line ratio for the three galaxies with anomalous Brackett-line line ratios, IRAS 10494+4424, IRAS 10565+2448, and Mrk 273.

We estimated the flux of the H $_2$ (1,0) O(2) line ($F_{\text{O}(2)}$) using another molecular hydrogen rotation-vibration line, H $_2$ (1,0) O(3), which has a rest wavelength of 2.802 μm and which is simultaneously detected in our observations. Black & van Dishoeck (1987) calculated the flux ratios of molecular hydrogen rotation-vibration lines both for fluorescence excitation and shock excitation. In previous ground-based K -band observations, the H $_2$ lines were shown to be thermally excited at a temperature of ~ 2000 K in IRAS 10494+4424 (Murphy et al. 2001), IRAS 10565+2448, and Mrk 273 (Goldader et al. 1997). Thus, we adopt the flux ratio $F_{\text{O}(2)} = 0.26F_{\text{O}(3)}$ from the shock model ($T = 2000$ K) of Black & van Dishoeck (1987), where $F_{\text{O}(3)}$ is the flux of the H $_2$ (1,0) O(3) line.

We measured $F_{\text{O}(3)}$ for the three galaxies that show anomalous Brackett-line ratios using Gaussian fitting. We fixed the width and central wavelength of the Gaussian profile and used the normalization of the Gaussian profile and the linear continuum as free parameters. Figure 6 shows the results of the Gaussian fitting of the H $_2$ (1,0) O(3) line. We detected the H $_2$ (1,0) O(3) line with moderate significance ($> 2.8\sigma$) in all three galaxies. The measured flux is summarized in Table 3, along with the 1σ statistical error. The 1σ systematic error is estimated to be $\sim 10\%$ of the flux.

Using the H $_2$ (1,0) O(3) line flux, we determined the H $_2$ (1,0) O(2) line flux, subtracted it from the Br β line flux, and calculated the flux ratio of the pure Br β line to the Br α line. We summarize the results in Table 3 ($F_{\text{Br}\beta}^{\text{cor}}/F_{\text{Br}\alpha}$). The ratio is still more than 3σ higher than the case B value of 0.565 for IRAS 10565+2448 and Mrk 273. Thus, contamination of the Br β line does not provide a full explanation of the anomalous line ratio at least for these galaxies. For IRAS 10494+4424, the significance of the anomaly is 2.7σ after the correction of the H $_2$ line. Hence, the detection of an anomalous line ratio in this ULIRG is admittedly not as robust as those in the other two, but it is still moderately significant. We thus retain this galaxy in the discussion

Table 3. Correction for Contamination by Molecular Hydrogen Line

Object Name	(Observed)	(Predicted)	
	$F_{\text{O}(3)}$ (10^{-15} erg s $^{-1}$ cm $^{-2}$)	$F_{\text{O}(2)}^a$	$F_{\text{Br}\beta}^{\text{cor}}/F_{\text{Br}\alpha}^b$
IRAS 10494+4424	2.79 ± 0.92	0.72 ± 0.24	0.89 ± 0.12
IRAS 10565+2448	5.2 ± 1.9	1.36 ± 0.49	0.845 ± 0.085
Mrk 273	25.6 ± 3.0	6.66 ± 0.79	0.952 ± 0.054

^aFlux of the H₂ (1,0) O(2) line derived from the H₂ (1,0) O(3) line assuming $F_{\text{O}(2)} = 0.26F_{\text{O}(3)}$ (2000 K shock model of [Black & van Dishoeck 1987](#)).

^bBr β /Br α line ratio corrected for contamination by the molecular hydrogen line. The predicted flux of the H₂ (1,0) O(2) line is subtracted from the observed flux of the Br β line.

below. We conclude that the anomalous Br β /Br α ratio is real and that conditions intrinsic to the ionized gas itself make the ratio anomalous.

In summary, for three out of 33 ULIRGs wherein we detected both the Br α and Br β lines, we found anomalous Br β /Br α line ratios. The ratios are significantly higher than the case B value even after the subtraction of possible contamination of the H₂ (1,0) O(2) line, at least in two sources, and are not explained by the effects of dust extinction. We also found that ULIRGs have a tendency to exhibit high Br β /Br α line ratios. As we discuss in Appendix B, the case B line ratio explains well the Br β /Br α line ratio in Galactic H II regions. This indicates that conditions in the H II regions in those ULIRGs with a Br β /Br α anomaly are entirely different from the conditions in Galactic H II regions.

4. INTERPRETATION OF THE ANOMALY

In this section, we discuss how to interpret the high Br β /Br α ratio. To investigate the H I line ratios, we first consider how the level populations of the hydrogen atoms are determined by assuming three possible excitation mechanisms: recombination, collisional excitation, and resonant excitation. Then, we discuss possible explanations for the high Br β /Br α ratio separately for optically thin and optically thick cases. In this section, we use the Einstein coefficients from [Johnson \(1972\)](#) and recombination coefficients from [Verner & Ferland \(1996\)](#).

4.1. Excitation Mechanisms for the Hydrogen Atoms

4.1.1. Recombination

As the first excitation mechanism, we discuss the recombination process. In the low-density limit, wherein collisions are negligible, the hydrogen level populations

are determined by recombination and radiative transitions. In this case, the equilibrium equation for the level population of a state with principal quantum number \mathcal{N} can be written as

$$n_p n_e \alpha_{\mathcal{N}} + \sum_{\mathcal{N}'=\mathcal{N}+1}^{\infty} n_{\mathcal{N}'} A_{\mathcal{N}',\mathcal{N}} = n_{\mathcal{N}} \sum_{\mathcal{N}''=2}^{\mathcal{N}-1} A_{\mathcal{N},\mathcal{N}''}, \quad (1)$$

where n_p , n_e , and $n_{\mathcal{N}}$ are the number densities of protons, electrons, and hydrogen atoms in quantum state \mathcal{N} , respectively; $\alpha_{\mathcal{N}}$ is the recombination coefficient for level \mathcal{N} ; and $A_{\mathcal{N}',\mathcal{N}}$ is the Einstein A coefficient for the $\mathcal{N}' \rightarrow \mathcal{N}$ transition. We assume case B conditions ([Osterbrock & Ferland 2006](#)), for which the Lyman lines are taken to be optically thick, so that the summation on the right-hand side ends at $\mathcal{N}'' = 2$.

Using the cascade matrix $C_{\mathcal{N}',\mathcal{N}}$, which is the probability that a population in level \mathcal{N}' undergoes a transition to level \mathcal{N} via all possible routes ([Seaton 1959](#)), we can rewrite Equation (1) as

$$n_{\mathcal{N}} A_{\mathcal{N}} = n_p n_e \sum_{\mathcal{N}'=\mathcal{N}}^{\infty} \alpha_{\mathcal{N}'} C_{\mathcal{N}',\mathcal{N}}, \quad (2)$$

where we have written $\sum_{\mathcal{N}''=2}^{\mathcal{N}-1} A_{\mathcal{N},\mathcal{N}''} = A_{\mathcal{N}}$. Thus, we have

$$\frac{n_{\mathcal{N}}}{n_{\mathcal{N}'}} = \frac{A_{\mathcal{N}'}}{A_{\mathcal{N}}} \frac{\sum_{l=\mathcal{N}}^{\infty} \alpha_l C_{l,\mathcal{N}}}{\sum_{l'=\mathcal{N}'}^{\infty} \alpha_{l'} C_{l',\mathcal{N}'}} \quad (3)$$

for the ratio of the level populations of states \mathcal{N} and \mathcal{N}' . The cascade matrix can be written in terms of the Einstein coefficients, which do not depend on gas properties such as temperature. The recombination coefficients depend weakly on temperature; however, in Equation (3), this dependence is almost canceled out because we have

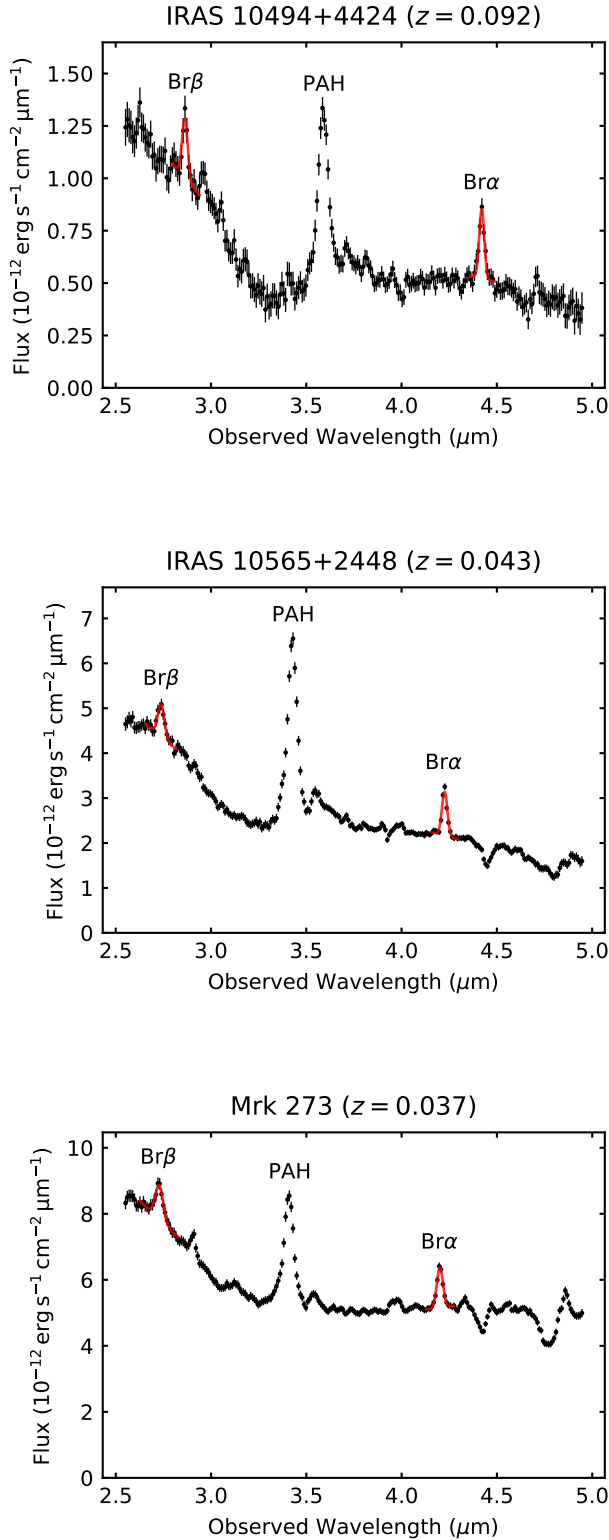


Figure 3. The 2.5–5.0 μm near-infrared spectra of galaxies that show $\text{Br}\beta/\text{Br}\alpha$ line ratios significantly higher than that for case B. The best-fit Gaussian profiles for the $\text{Br}\alpha$ and $\text{Br}\beta$ lines are plotted as red curves.

the coefficients both in the numerator and the denominator. Thus, the level population depends only weakly on temperature for the case in which it is determined by the recombination process.

4.1.2. Collisional Excitation

Next, we consider the collisional excitation mechanism. In the high-density limit, wherein the level population is entirely determined by collisions, the level population reaches thermal equilibrium and follows the Boltzmann distribution. The ratio of level populations for this case can be written as

$$\frac{n_{\mathcal{N}}}{n_{\mathcal{N}'}} = \frac{g_{\mathcal{N}}}{g_{\mathcal{N}'}} \frac{\exp\left(-\frac{E_{\mathcal{N}}}{kT}\right)}{\exp\left(-\frac{E_{\mathcal{N}'}}{kT}\right)}, \quad (4)$$

where $g_{\mathcal{N}}$ is the degeneracy of state \mathcal{N} , k is Boltzmann's constant, $E_{\mathcal{N}}$ is the energy of state \mathcal{N} relative to the ground state, and T is the gas temperature. The critical densities for transitions $\mathcal{N} = 1 \rightarrow 5$ and 6 are on the order of $\sim 10^{11} \text{ cm}^{-3}$ (Storey & Hummer 1995); therefore, gas densities higher than this threshold are required to achieve thermal equilibrium for the levels related to the $\text{Br}\alpha$ and $\text{Br}\beta$ line emissions.

4.1.3. Resonant Excitation

The third excitation mechanism is resonant excitation. One example wherein this process becomes important is the Bowen resonance of O III lines (Osterbrock & Ferland 2006). The wavelength of the O III $2p^2 \ ^3P_2 - 3d^3 \ ^3P_2^o$ line (303.80 \AA) is accidentally coincident with that of the He II $\text{L}\alpha$ line (303.78 \AA); therefore, the $3d^3 \ ^3P_2^o$ level of O III is pumped by the He II $\text{L}\alpha$ line. This results in an enhancement of the O III lines originating from the $3d^3 \ ^3P_2^o$ state. A similar situation would occur for hydrogen lines if a line were to exist with a wavelength close to that of the $\mathcal{N} = \mathcal{N}' \rightarrow 1$ transitions, i.e., the Lyman series. In this case, the line will pump the electrons from the hydrogen ground state to state \mathcal{N}' , resulting in an enhancement of the level population of the \mathcal{N}' state.

Based on the three excitation mechanisms described above, we consider some possible explanations for the high $\text{Br}\beta/\text{Br}\alpha$ line ratios.

4.2. Optically Thin Case

We first consider the case in which the Brackett lines are optically thin. In this case, once the level population of neutral hydrogen is determined, the flux ratios of the H I lines are fixed. The emergent $\text{Br}\beta/\text{Br}\alpha$ line ratio is then

$$\frac{F_{\text{Br}\beta}}{F_{\text{Br}\alpha}} = \frac{n_6}{n_5} \frac{A_{\text{Br}\beta}}{A_{\text{Br}\alpha}} \frac{h\nu_{\text{Br}\beta}}{h\nu_{\text{Br}\alpha}} \sim 0.440 \frac{n_6}{n_5}, \quad (5)$$

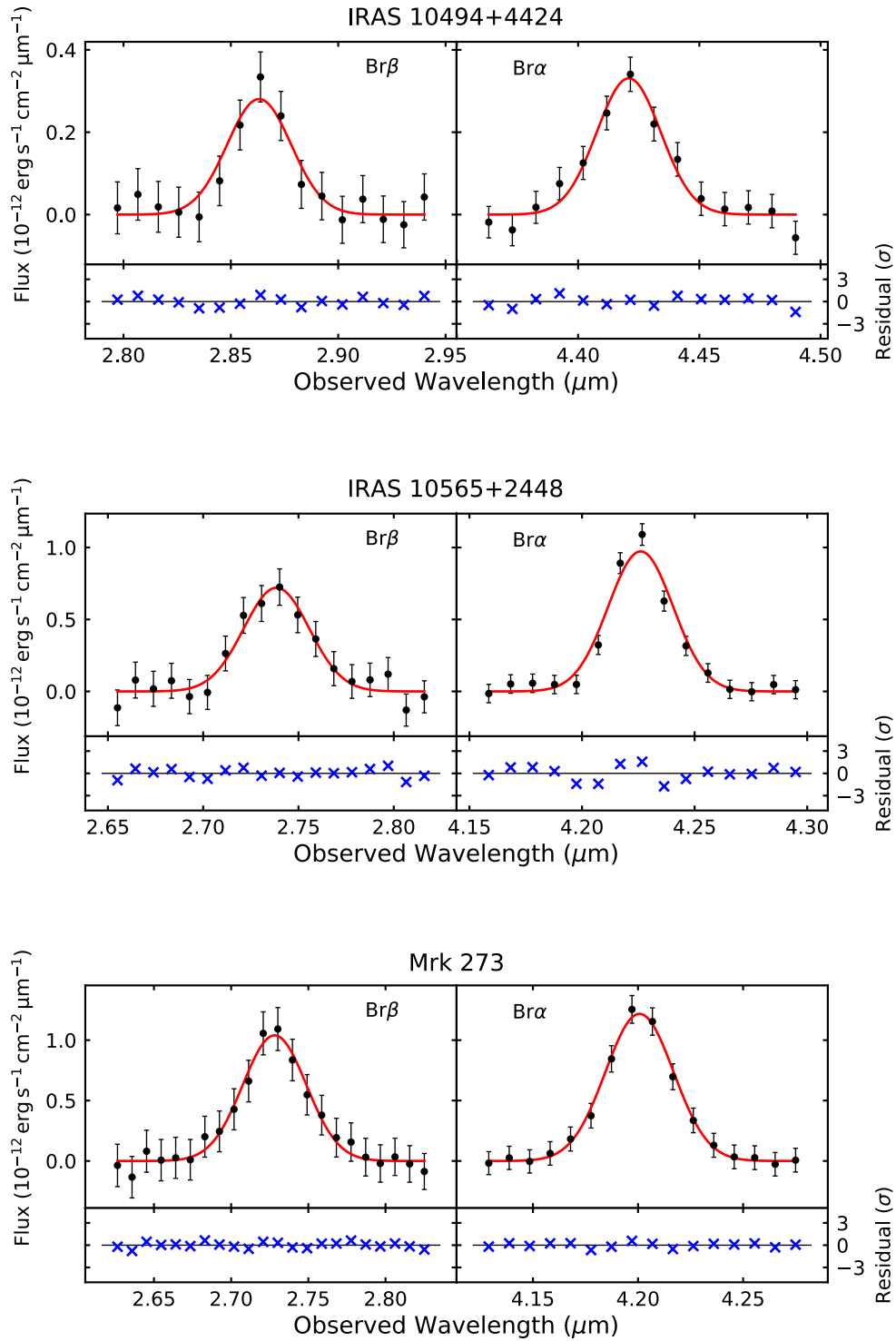


Figure 4. Spectra around the Br α (right) and Br β (left) lines for the three galaxies that show anomalous Br β /Br α line ratios. The underlying continuum has been subtracted. The best-fit Gaussian profile is plotted as a solid red curve. The residuals from the best fit are also displayed in the bottom panels using blue crosses.

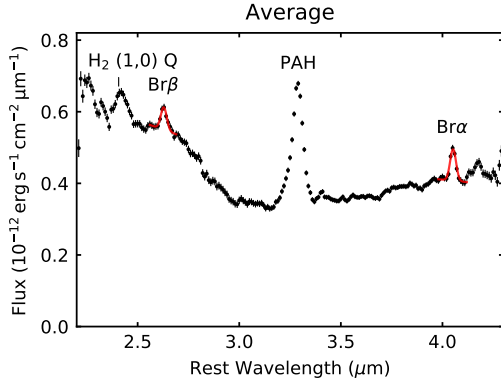


Figure 5. Averaged near-infrared spectrum of 35 galaxies with $F_{\text{Br}\alpha} < 10^{-14}$ erg s $^{-1}$ cm $^{-2}$. The best-fit Gaussian profiles for the Br α and Br β lines are plotted as red curves.

where n_6/n_5 is the ratio of the populations of hydrogen atoms in levels $\mathcal{N} = 6$ and $\mathcal{N} = 5$, A_{line} is the Einstein A coefficient for the line, h is Planck's constant, and ν_{line} is the frequency of the line. This equation shows that in order to explain a high Br β /Br α line ratio, the level population in $\mathcal{N} = 6$ must be enhanced relative to that in $\mathcal{N} = 5$.

At low densities, where the recombination process is dominant, the level populations are determined by Equation (3). Assuming $T = 10000$ K as the gas temperature, we obtain $F_{\text{Br}\beta}/F_{\text{Br}\alpha} = 0.565$, i.e., the case B ratio, by substituting Equation (3) into Equation (5). In contrast, in the high-density limit where the collisional process is dominant, the hydrogen level populations are determined by Equation (4). Again, assuming $T = 10000$ K as the gas temperature, we obtain $F_{\text{Br}\beta}/F_{\text{Br}\alpha} = 0.522$ by substituting Equation (4) into Equation (5). If we take the limit $T \rightarrow \infty$, Equation (4) gives $n_6/n_5 = g_6/g_5 = 1.44$ as the high- T limit, and we obtain $F_{\text{Br}\beta}/F_{\text{Br}\alpha} = 0.634$. This is the highest line ratio achievable with collisional excitation but it is still lower than the observed values. Thus, we cannot explain the high Br β /Br α line ratios in either the high-density or the low-density limits.

In general, the level populations are affected both by the recombination and collisional process, so the combined results are expected to lie somewhere between the above two limits. This is expressed in terms of the departure coefficient $b_{\mathcal{N}}$, which is the fractional departure of the population of state \mathcal{N} from that in thermal equilibrium, $n_{\mathcal{N}}^{\text{th}}$; i.e., $n_{\mathcal{N}} = b_{\mathcal{N}} n_{\mathcal{N}}^{\text{th}}$. Storey & Hummer (1995) calculated the $b_{\mathcal{N}}$ coefficients for several gas densities, and we show their results in Figure 7. Hereafter, we denote the total hydrogen number density by n ; i.e., we write $n(\text{H}^0) + n(\text{H}^+) = n$, where $n(\text{H}^0)$ and $n(\text{H}^+)$ are the number densities of neutral and ionized hydro-

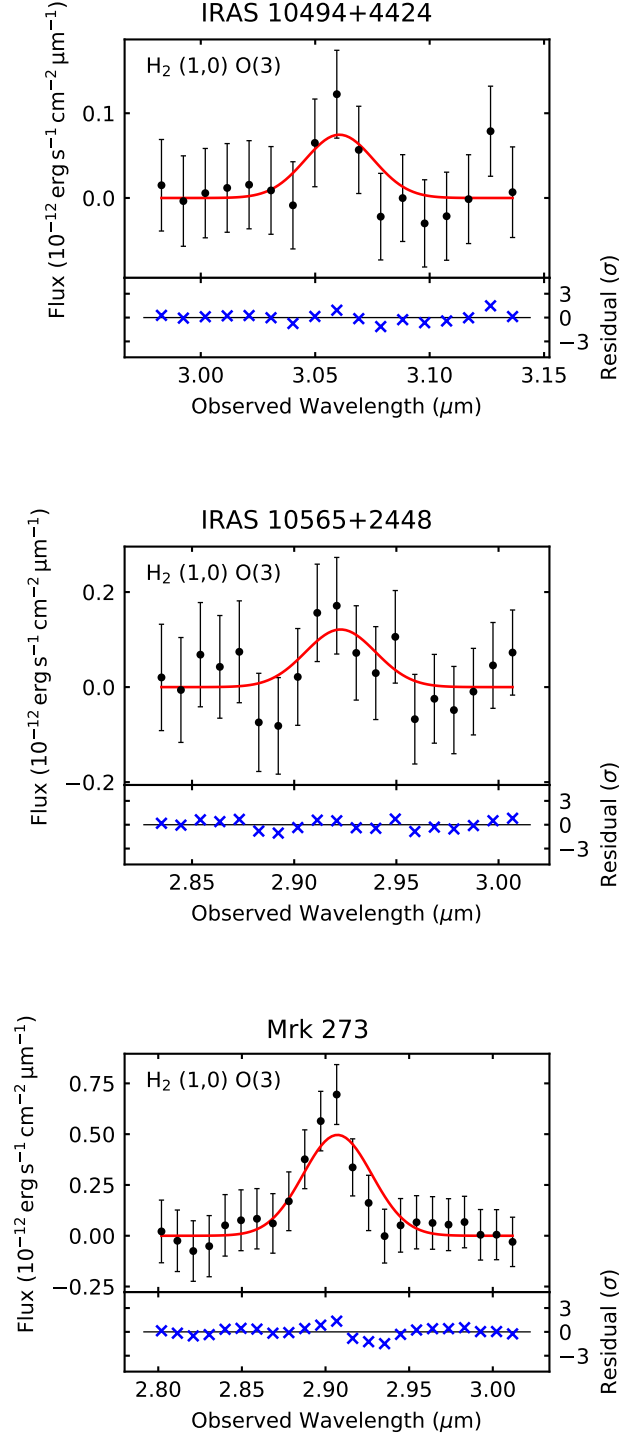


Figure 6. Spectra around the H $_2$ (1,0) O(3) line. The underlying continuum has been subtracted. The best-fit Gaussian profile is plotted as a solid red curve. The residuals from the best fit are also displayed in the bottom panels using blue crosses.

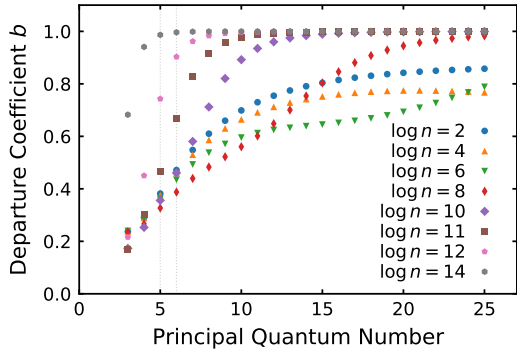


Figure 7. Departure coefficients for hydrogen atoms in states $\mathcal{N} \leq 25$ for various total hydrogen densities n at $T = 10000$ K assuming case B conditions (data taken from Storey & Hummer 1995). The levels $\mathcal{N} = 5$ and 6 are denoted with gray dotted lines.

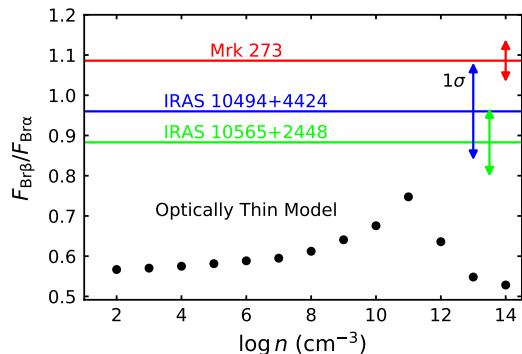


Figure 8. The $F_{\text{Br}\beta}/F_{\text{Br}\alpha}$ ratio for the optically thin case, for various total hydrogen densities n . The horizontal red, green, and blue lines show the observed $F_{\text{Br}\beta}/F_{\text{Br}\alpha}$ ratios for Mrk 273, IRAS 10565+2448, and IRAS 10494+4424, respectively. The 1σ uncertainty ranges are shown by the vertical arrows.

gen, respectively. In the ionized gas, we assume that the hydrogen atoms are fully ionized, so that $n_e \sim n$. The level populations for $\mathcal{N} = 6$ and $\mathcal{N} = 5$ are affected by the collisional process for densities higher than the critical density $n \sim 10^{11} \text{ cm}^{-3}$.

Using the $b_{\mathcal{N}}$ coefficients, we can determine the n_6/n_5 ratio for each gas density and so derive the $\text{Br}\beta/\text{Br}\alpha$ line ratio from Equation (5). We show these results in Figure 8. At low densities, the $\text{Br}\beta/\text{Br}\alpha$ line ratio is consistent with the case B ratio. When the density becomes $n \geq 10^{10} \text{ cm}^{-3}$, collisional excitation starts to contribute to the $\mathcal{N} = 6$ state. This causes an enhancement of the $\text{Br}\beta$ line. At densities higher than $n \geq 10^{12} \text{ cm}^{-3}$, the $\mathcal{N} = 5$ state also begins to be collisionally excited, and so the $\text{Br}\beta/\text{Br}\alpha$ line ratio approaches the ratio in thermal equilibrium.

Figure 8 indicates that the $\text{Br}\beta/\text{Br}\alpha$ line ratio becomes as high as ~ 0.75 at $n \sim 10^{11} \text{ cm}^{-3}$. This ratio is within 1.6σ and 1.8σ of the observed ratios for IRAS 10565+2448 (0.88 ± 0.09) and IRAS 10494+4424 (0.96 ± 0.12), respectively, but it is still more than 3σ lower than that observed in Mrk 273 (1.09 ± 0.05). Thus, we conclude that we cannot explain the anomaly with just the recombination and collisional processes in the optically thin case.

With resonant excitation, the $\mathcal{N} = 6$ state is enhanced if a strong line with a wavelength comparable to that of the transition $\mathcal{N} = 6 \rightarrow 1$ (937.8 \AA) exists. As we discuss in detail in Appendix C.1, we found that if this (unknown) line have a transition probability comparable to those of forbidden lines, then the resonant process would be able to make the $\text{Br}\beta/\text{Br}\alpha$ line ratio anomalously high.

We reviewed the atomic and molecular data currently available to search for possible resonant lines. For the line data, we used the line list provided in the Cloudy program (Ferland et al. 1998). Cloudy is a spectral-synthesis code designed to numerically simulate an astrophysical plasma and its emissions. Extensive atomic and molecular data are collected in the code (references are available in a file distributed along with the code). We searched for possible resonant lines with a wavelength of $\sim 937.8 \text{ \AA}$ within a velocity range of $\sim 10 \text{ km s}^{-1}$, corresponding to the thermal velocity at $T = 10000 \text{ K}$ (Osterbrock & Ferland 2006). We found no candidates in the Cloudy data, and thus we exclude this resonant process as a possible cause of the anomalous $\text{Br}\beta/\text{Br}\alpha$ line ratio.

Based on the above discussion, we conclude that we cannot explain the anomalous $\text{Br}\beta/\text{Br}\alpha$ line ratio if the Brackett lines are optically thin.

4.3. Optically Thick Case

The alternative is that the Brackett lines are optically thick and the observed line ratio deviates from Equation (5). In this case, it is possible to explain the high $\text{Br}\beta/\text{Br}\alpha$ line ratio if the $\text{Br}\alpha$ line becomes optically thick and saturates, whereas the $\text{Br}\beta$ line remains optically thin. Herein, we discuss the optical-depth effect on this ratio.

4.3.1. Optical Depth of Brackett Lines

In a uniform gas, the optical depth $\tau_{\mathcal{N}',\mathcal{N}}$ at the line center for the transition $\mathcal{N}' \rightarrow \mathcal{N}$ is given as

$$\tau_{\mathcal{N}',\mathcal{N}} = \int_0^R \alpha_{\mathcal{N},\mathcal{N}'} n_{\mathcal{N}} dl \sim \alpha_{\mathcal{N},\mathcal{N}'} N_{\mathcal{N}}, \quad (6)$$

where R is the size of the gas, $\alpha_{\mathcal{N},\mathcal{N}'}$ is the absorption cross-section of the transition $\mathcal{N} \rightarrow \mathcal{N}'$, $n_{\mathcal{N}}$ is the num-

ber density of neutral hydrogen in state \mathcal{N} , and $N_{\mathcal{N}}$ is the column density of neutral hydrogen in state \mathcal{N} . The optical depth of the Brackett lines is proportional to the column density of neutral hydrogen in the quantum state $\mathcal{N} = 4$.

Assuming a Gaussian profile as a line velocity profile, the absorption cross-section is related to the Einstein B coefficient, $B_{\mathcal{N},\mathcal{N}'}$, by

$$\alpha_{\mathcal{N},\mathcal{N}'} = \frac{hc}{4\pi^{3/2}} \frac{B_{\mathcal{N},\mathcal{N}'}}{v_{\text{Dop}}}, \quad (7)$$

where c is the speed of light, and v_{Dop} is the Doppler velocity half width, the distance from line center where the line profile falls to e^{-1} of its peak. If the line profile is determined solely by thermal motions, the Doppler width can be written as $v_{\text{Dop}} = v_{\text{Therm}} = \sqrt{2kT/m_{\text{H}}}$, where m_{H} is the mass of a hydrogen atom. At $T = 10000$ K, we have $v_{\text{Therm}} \sim 13$ km s $^{-1}$. If a turbulent motion with a velocity v_{Turb} affects the line width, $v_{\text{Dop}} = \sqrt{v_{\text{Therm}}^2 + v_{\text{Turb}}^2}$.

Substituting Equation (7) into Equation (6) and assuming $T = 10000$ K, we obtain the line optical depths of the Br α and Br β lines as

$$\tau_{\text{Br}\alpha} \sim 1.0 \left(\frac{N_4}{1.6 \times 10^{11} \text{ cm}^{-2}} \right) \left(\frac{v_{\text{Dop}}}{10 \text{ km s}^{-1}} \right)^{-1}, \quad (8)$$

$$\tau_{\text{Br}\beta} \sim 0.11 \left(\frac{N_4}{1.6 \times 10^{11} \text{ cm}^{-2}} \right) \left(\frac{v_{\text{Dop}}}{10 \text{ km s}^{-1}} \right)^{-1}. \quad (9)$$

Thus, assuming $v_{\text{Dop}} \sim 10$ km s $^{-1}$, for instance, we find that the Br α line becomes optically thick while the Br β line is still optically thin when $N_4 \sim 2 \times 10^{11}$ cm $^{-2}$. We further discuss the possible conditions that can produce a high Br β /Br α line ratio on the basis of Equations (8) and (9).

4.3.2. Possible Conditions Producing a High Brackett-Line Ratio

Herein, we assume that the high Br β /Br α line ratio is produced within a single isolated H II region ionized by a single star and that what we observe is an ensemble of such H II regions. Within a single H II region, we assume that v_{Dop} is determined only by the thermal width, with $v_{\text{Therm}} \sim 10$ km s $^{-1}$, which is a typical velocity observed in nearby H II regions (e.g., Arthur et al. 2016). We assume that the Br α line becomes optically thick within each H II region.

For a spherical and uniform H II region, we next discuss how to make the Br α line optically thick using the three excitation mechanisms described in §4.1. First, we consider the case in which the recombination process is dominant. In this case, n_4 is determined by Equation (2), which yields $n_4 \sim 3.6 \times 10^{-21} (n/\text{cm}^{-3})^2 \text{ cm}^{-3}$.

We can thus write N_4 in terms of n and R as

$$N_4 = n_4 R \sim 3.6 \times 10^{-21} \left(\frac{n}{\text{cm}^{-3}} \right)^2 \left(\frac{R}{\text{cm}} \right) \text{ cm}^{-2}. \quad (10)$$

If we write $nR = N$, where N is the total hydrogen column density, then we have

$$N_4 = 3.6 \times 10^{-21} \left(\frac{n}{\text{cm}^{-3}} \right) \left(\frac{N}{\text{cm}^{-2}} \right) \text{ cm}^{-2}. \quad (11)$$

Thus N_4 is proportional to both n and N . If the H II region is ionized by a central star that emits the number of ionizing photons per unit time $Q(\text{H})$, then ionization-equilibrium at $T = 10000$ K yields

$$Q(\text{H}) = \int \alpha_{\text{B}} n_{\text{e}} n_{\text{p}} dV \sim \frac{4\pi}{3} \alpha_{\text{B}} n^2 R^3 = \frac{4\pi}{3} \alpha_{\text{B}} N^3 n^{-1},$$

$$\therefore N = 3.37 \times 10^{20} \left(\frac{Q(\text{H})}{10^{49} \text{ s}^{-1}} \right)^{\frac{1}{3}} \left(\frac{n}{\text{cm}^{-3}} \right)^{\frac{1}{3}} \text{ cm}^{-2}, \quad (12)$$

where α_{B} is the total recombination coefficient for hydrogen in case B, and $Q(\text{H}) = 10^{49}$ s $^{-1}$ is a typical value for an O star (Osterbrock & Ferland 2006). Substituting Equation (12) into Equation (11), we obtain N_4 in terms of n and $Q(\text{H})$;

$$N_4 = 2.35 \times 10^{11} \times \left(\frac{Q(\text{H})}{10^{49} \text{ s}^{-1}} \right)^{\frac{1}{3}} \left(\frac{n}{10^8 \text{ cm}^{-3}} \right)^{\frac{4}{3}} \text{ cm}^{-2}. \quad (13)$$

Thus, within a single H II region with an ionizing source emitting $Q(\text{H}) \sim 10^{49}$ s $^{-1}$, a gas density as high as $n \sim 10^8$ cm $^{-3}$ is required to achieve a column density $N_4 \sim 2 \times 10^{11}$ cm $^{-2}$ that is large enough to make the Br α line optically thick.

At a density $n = 10^8$ cm $^{-3}$, the collisional process is not dominant as the excitation mechanism for the population in the quantum state $\mathcal{N} = 4$ because the critical density for the $\mathcal{N} = 1 \rightarrow 4$ transition is $\sim 10^{12}$ cm $^{-3}$ (Storey & Hummer 1995). This is also shown in Figure 7. The relative difference between the b_4 coefficients at $n = 10^8$ cm $^{-3}$ and at 10^2 cm $^{-3}$ is less than 10%, indicating that the $\mathcal{N} = 4$ state is not dominantly populated by the collisional process at densities $n \leq 10^8$ cm $^{-3}$. Thus, Equation (13), in which only the recombination process is considered, is valid if we take collisional excitation into account at a density of $n = 10^8$ cm $^{-3}$.

Resonant excitation would enhance the $\mathcal{N} = 4$ state if a line exists with a wavelength equal to that of the $\mathcal{N} = 4 \rightarrow 1$ transition (972.5 Å). In this case, the density required to make the Br α line optically thick would be lowered from the value $n \sim 10^8$ cm $^{-3}$ given by Equation (13). Based on a detailed discussion provided in

Appendix C.2, we found that if a line with a wavelength of $\sim 972.5 \text{ \AA}$ and a transition probability of $\sim 10^{-1} \text{ s}^{-1}$ exists, we should take the resonant process into consideration in determining the population of the $\mathcal{N} = 4$ state.

We searched for possible resonant lines with wavelengths of $\sim 972.5 \text{ \AA}$ within the velocity range $\sim 10 \text{ km s}^{-1}$, which corresponds to the thermal velocity at $T = 10000 \text{ K}$ (Osterbrock & Ferland 2006) using the line list from the Cloudy code (Ferland et al. 1998) and found no candidates for the X_4 line. Thus, we conclude that the resonant process does not take place and is excluded from the excitation mechanisms for the $\mathcal{N} = 4$ state.

4.3.3. Simulation with Cloudy

In order to investigate quantitatively the $\text{Br}\beta/\text{Br}\alpha$ line ratio taking all excitation mechanisms into account, we used the Cloudy code (ver. 10.00; Ferland et al. 1998) and simulated the ratio for the optically thick case. Cloudy calculates the recombination and the collisional processes altogether. Cloudy also solves the radiative transfer of lines and so can be used to investigate the effect of optical depth on the line fluxes.

To execute a simulation with Cloudy, four parameters are required: (1) the spectral shape of the incident radiation, (2) the intensity of the incident radiation, (3) the density of the surrounding gas, and (4) the criterion for stopping the calculation. We considered a single spherical H II region with a uniform gas ionized by a hot central star. For the spectral shape of the incident radiation (1), we used 40000 K blackbody radiation to simulate a typical O star (Osterbrock & Ferland 2006). For the intensity of the incident radiation (2), we specified the number of ionizing photons per unit time, $Q(\text{H})$. We varied $Q(\text{H})$ from 10^{48} s^{-1} to 10^{51} s^{-1} using intervals of a decade on the assumption that the ionizing radiation is dominated by massive OB stars in starburst regions. The $Q(\text{H})$ values 10^{48} s^{-1} , 10^{49} s^{-1} , and 10^{50} s^{-1} correspond to typical values for B stars, O5 stars, and massive O stars (O3 stars), respectively (Osterbrock & Ferland 2006). We also calculated a case with $Q(\text{H}) = 10^{51} \text{ s}^{-1}$ for reference. We varied the gas density (3) from $n = 10^5 \text{ cm}^{-3}$ to 10^{10} cm^{-3} using intervals of a decade. To simulate line emission from the ionized region, we adopted the electron fraction for the total gas, i.e., the degree of ionization, to be 0.1 as the stopping criterion for the calculation (4). In addition to the abovementioned parameters, we specified a spherical geometry with the inner radius of the surrounding gas, which is required in Cloudy when we use $Q(\text{H})$ as the intensity of the incident radiation, equal to $r = 10^{12} \text{ cm}$.

We iterated the calculations until the difference between the line optical depths of the last two iterations became smaller than 0.20. The adopted parameters described above are summarized in Table 4. Other parameters are set to the default values of Cloudy; e.g., the line width is determined by the thermal velocity, solar abundances are adopted, and dust grains are not included in the calculations.

The results of the Cloudy simulations of the $\text{Br}\beta/\text{Br}\alpha$ line ratio are shown in Figure 9. We find that the $\text{Br}\beta/\text{Br}\alpha$ line ratio increases for high values of n and N . In contrast, the ratio is close to the case B value (0.565) for low values of n and N . The optical depth of the $\text{Br}\alpha$ line is proportional to N_4 , which is proportional to n and N , as shown in Equation (11). Thus, the results are consistent with our simple estimate, indicating that a high $\text{Br}\beta/\text{Br}\alpha$ line ratio is produced when the $\text{Br}\alpha$ line becomes optically thick.

We now compare the observed $\text{Br}\beta/\text{Br}\alpha$ line ratios with the Cloudy results. Figure 9 indicates that the observed ratios in the three galaxies are consistent with $n \sim 10^8 \text{ cm}^{-3}$, where the $\text{Br}\alpha$ line starts to become optically thick. In conditions with higher values of n , the $\text{Br}\beta/\text{Br}\alpha$ line ratio becomes too large to match the observed anomalies. From this result, we conclude that in order to explain the observed $\text{Br}\beta/\text{Br}\alpha$ line ratio within a single H II region, gas densities as high as $n \sim 10^8 \text{ cm}^{-3}$ are required to achieve column densities large enough to make the $\text{Br}\alpha$ line optically thick.

5. COMPARISON WITH OTHER HYDROGEN RECOMBINATION LINES

In Cloudy simulations, not only $\text{Br}\alpha$ and $\text{Br}\beta$, but also other H I recombination lines are calculated. The intensity ratios between those lines can also be compared to observations. We here review the existing observations of other H I lines in the optical and near-infrared for the ULIRGs, in particular for the three objects in which significant anomalous $\text{Br}\beta/\text{Br}\alpha$ ratios were found, and demonstrate that they do not contradict the predictions of our high-density model. This also explains why intensity ratio anomalies such as the one revealed in this work have not been found before. In the following subsections, we explain the reasons in detail for each H I line of interest. A basic short explanation is that even if the intensity ratio of other H I lines deviates from the case B value due to the high-density condition, that change is indistinguishable from the effect of attenuation.

As a reference model for explaining the observed $\text{Br}\beta/\text{Br}\alpha$ line ratio, we adopt the Cloudy result calculated for $n = 10^8 \text{ cm}^{-3}$ and $Q = 10^{50} \text{ s}^{-1}$. This model represents an H II region, ionized by an O3 star

Table 4. Parameters Used in Cloudy Simulations^a

Parameter	Value	Description
Blackbody	40000 K	Spectral shape of incident radiation.
$\log Q(\text{H})^b$	48–51	Intensity of incident radiation.
$\log r^c$	12	Inner radius of surrounding gas.
$\log n^d$	5–10	Density of surrounding gas.
Stop Efrac ^e	–1	Stopping criterion for calculation.
Sphere	...	Geometry of surrounding gas.
Iterate to Convergence ^f	0.20	Stopping criterion for iteration.

^aAll input parameters we used for the calculations are listed. Other parameters were set to the default values of Cloudy.

^bLog of the number of ionizing photons in s^{-1} .

^cLog of the inner radius of the gas in cm.

^dLog of the total hydrogen number density of the gas in cm^{-3} .

^eLog of the electron fraction below which the calculation stops.

^fThe calculation is iterated until the difference between the optical depths of the last two iterations becomes smaller than the specified value.

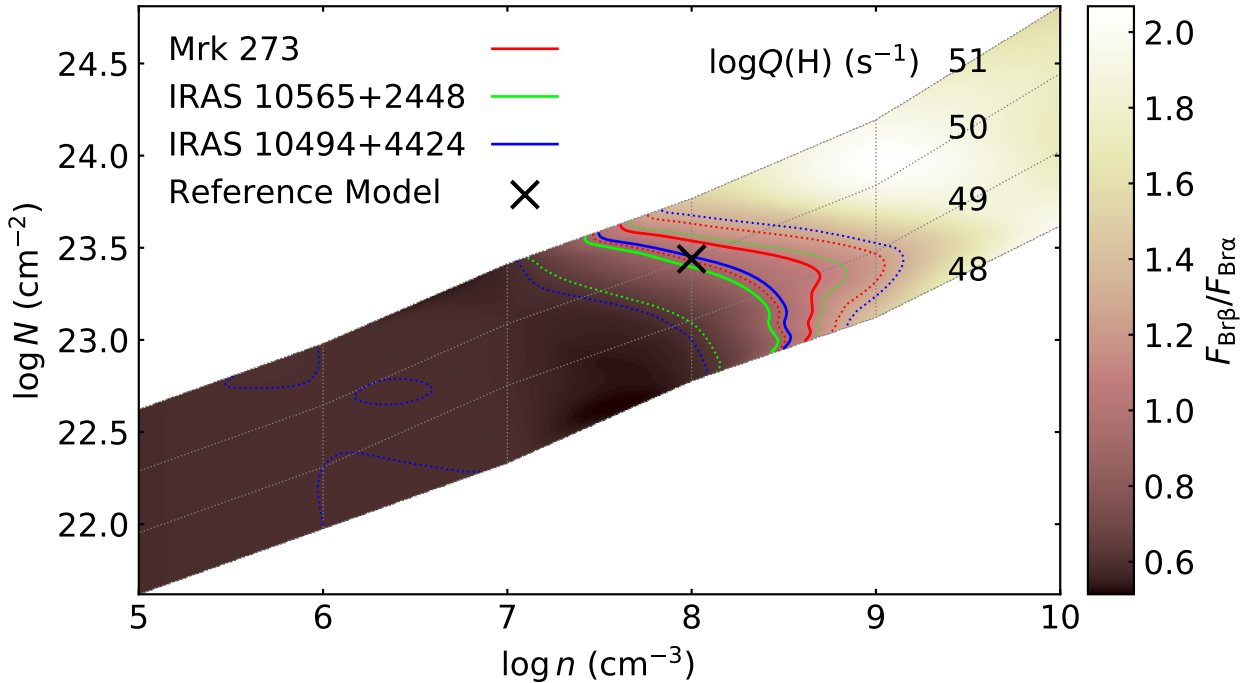


Figure 9. Cloudy result for the $\text{Br}\beta/\text{Br}\alpha$ line ratios. The number of ionizing photons $Q(\text{H})$ and the total hydrogen density n are varied within the ranges $10^{48} \text{ s}^{-1} \leq Q(\text{H}) \leq 10^{51} \text{ s}^{-1}$ and $10^5 \text{ cm}^{-3} \leq n \leq 10^{10} \text{ cm}^{-3}$ using intervals of a decade. The $\text{Br}\beta/\text{Br}\alpha$ line ratio is shown as the color scale. The observed $\text{Br}\beta/\text{Br}\alpha$ line ratios for Mrk 273, IRAS 10565+2448, and IRAS 10494+4424 are presented as red, green, and blue lines, respectively. The observed values are shown by the solid lines, and the ranges of 3σ uncertainties are indicated by the dotted lines. The model calculated with $Q(\text{H}) = 10^{50} \text{ s}^{-1}$ and $n = 10^8 \text{ cm}^{-3}$ is indicated by the black cross.

Table 5. Summary of the reference model

Parameters	
Gas density	$n = 10^8 \text{ cm}^{-3}$
Incident radiation	$Q(\text{H}) = 10^{55} \text{ s}^{-1}$
Results	
Column density	$N = 2.75 \times 10^{23} \text{ cm}^{-2}$
Br α luminosity	$L_{\text{Br}\alpha} = 2.79 \times 10^{36} \text{ erg s}^{-1}$
Br β /Br α ratio	$F_{\text{Br}\beta}/F_{\text{Br}\alpha} = 0.940$
Case B value	$F_{\text{Br}\beta}/F_{\text{Br}\alpha} = 0.565$ (for reference)

and surrounded by gas at high density. The parameters and important results of this reference model are summarised in Table 5. The Br β /Br α line ratio for this model (0.940) explains well the observed values in IRAS 10494+4424, IRAS 10565+2448, and Mrk 273 of 0.96 ± 0.12 , 0.88 ± 0.09 , and 1.09 ± 0.05 , respectively. The predictions made by this model for several other H I line ratios, which are to be discussed below, are listed in Table 6. This table also shows the values for case B and the values observed in the three ULIRGs.

5.1. Comparison with H α Line

In this subsection, we compare the fluxes of the Brackett lines and the H α line for IRAS 10494+4424, IRAS 10565+2448, and Mrk 273. For IRAS 10494+4424 and Mrk 273, we use the H α line flux obtained from our Nickel observations (Table 2). IRAS 10565+2448 was observed with the integral field unit on the Gemini North telescope by Shih & Rupke (2010); they reported an integrated H α line flux $F_{\text{H}\alpha} = (8.42 \pm 0.84) \times 10^{-14} \text{ erg s}^{-1} \text{ cm}^{-2}$ for this galaxy (before extinction correction) within an aperture of $5'' \times 7''$. We adopt this flux for comparison with our results for IRAS 10565+2448.

We summarize the H α /Br α line ratio in Table 6. Figure 10 compares the flux of the Br α , Br β , and H α lines. The high-density model explains well both the H α /Br α and Br β /Br α line ratios if the dust extinction is $A_V \sim 2.5\text{--}5.0$ mag; this is higher than the typical value of $A_V \sim 1.3$ mag suggested by Kennicutt (1998) for typical spiral galaxies. The Br β /Br α line ratio is not much affected (reduced only by $\sim 10\text{--}20\%$), even for relatively high dust extinction. Thus, the high Br β /Br α line ratio predicted by the high-density model is clearly seen even with dust extinction of $A_V \sim 2.5\text{--}5.0$ mag, which explains well the observed ratios. In contrast, the H α /Br α line ratio is determined almost exclusively by the effect of dust extinction, and the difference between case B and the high-density model is small. The observed H α /Br α line ratio is consistent with the high-density model if

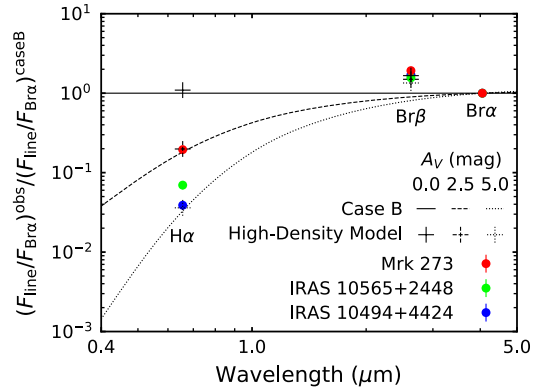


Figure 10. Hydrogen recombination-line fluxes relative to the Br α line. The ratios are normalized to those predicted for case B (10000 K, low-density limit: Osterbrock & Ferland 2006). The black lines show the line ratios for the case B model with different visual extinctions. The black crosses show the line ratios predicted by the high-density model. The solid, dashed, and dotted crosses indicate the ratios with no dust extinction, with extinction of $A_V = 2.5$ mag, and with extinction of $A_V = 5.0$ mag, respectively.

the dust extinction is $A_V \sim 2.5\text{--}5.0$ mag, and it is also explained by the case B model with almost the same dust extinction. We cannot distinguish between these two models from the H α /Br α line ratio.

We conclude that the high-density model is consistent with the observations of the H α line. The effect of dust extinction at optical wavelengths is so strong that the deviation of the H I line ratios from those of case B due to the high-density condition is easily cancelled out and made unnoticeable.

5.2. Comparison with H β /H α Line Ratio

The H β line ($\mathcal{N} = 4 \rightarrow 2$, 4861 Å) is also observable in the optical as well as H α , and the H β /H α line ratio is one of the most intensively studied ratios among H I lines (e.g., Kim et al. 1998). We here compare the H β /H α line ratio with our Br β /Br α line ratio.

For the AGNUL sample, we use the H β /H α line ratio summarized in Table 3 of Yano et al. (2016). The ratios for the two galaxies added to our sample in this paper are summarized in Appendix A. The H β /H α line ratios for all the targets are well below the case B value of 0.348 (Table 6). This indicates that the H β /H α line ratio can be explained with a combination of case B and dust extinction. The inferred dust extinction in this case (A_V^{opt} in the tables) is typically ~ 2.5 mag.

A comparison of the H β /H α line ratio with our Br β /Br α line ratio is shown in Figure 11 and displays a large scatter between the two ratios. The extinction vectors in Figure 11 indicate that the H β /H α line ratio is strongly affected by dust extinction. In contrast,

Table 6. Modeled and Observed H I Line Ratios

Lines	Case B	High-Density Model	IRAS 10494+4424	IRAS 10565+2448	Mrk 273
Br β /Br α	0.565	0.940	0.96 ± 0.12	0.88 ± 0.09	1.09 ± 0.05
H α /Br α	34.4	37.6	1.34 ± 0.17	2.39 ± 0.28	6.70 ± 0.69
H β /H α	0.348	0.216	0.110 ± 0.005	0.061 ± 0.003	0.100 ± 0.005
Pa α /Br γ	12.1	9.93	16.1 ± 1.5^a	...	10.8 ± 1.0^b

^aTaken from Murphy et al. (2001).

^bTaken from Veilleux et al. (1999b).

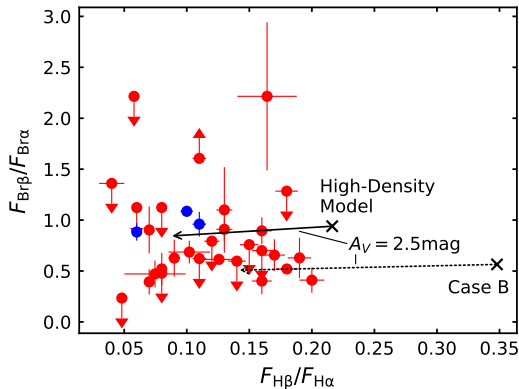


Figure 11. Br β /Br α line ratio versus H β /H α line ratio. The three galaxies with high Br β /Br α line ratios are represented by blue circles, while the others are shown as red circles. The black cross indicates the line ratios predicted by the high-density model. The extinction vectors for $A_V = 2.5$ mag are shown as the black arrows. The solid arrow shows extinction from the ratios of the high-density model, whereas the dashed arrow indicates extinction from the ratios of case B.

the Br β /Br α line ratio is almost unchanged with dust extinction of $A_V \sim 2.5$ mag.

The observed high Br β /Br α line ratios cannot be achieved by the case B model. In contrast, the extinction vector from the high-density model indicates that both the high Br β /Br α line ratio and the H β /H α line ratio are well explained by the high-density model with dust extinction of $A_V \sim 2.5$ mag.

In the high-density model, the H β /H α line ratio is predicted to be 0.216 (Table 6). We note that the deviation of the H β /H α line ratio in the high-density model is not distinguishable from the effect of dust extinction. This indicates that the deviation cannot be probed with the H β /H α line ratio even in conditions wherein dust extinction is very low.

From these results, we conclude that the high-density model is consistent with the observations of the H β /H α

line ratio. We also conclude that the deviation of the H I line ratios from those of case B can be observed only in the infrared, wherein the effect of dust extinction is small.

5.3. Comparison with Pa α /Br γ Line Ratio

In this subsection, we compare our results with infrared H I lines. In the infrared, the Br γ line at $2.17 \mu\text{m}$ and the Pa α line at $1.88 \mu\text{m}$ are both observable in K -band ($\sim 1.9\text{--}2.5 \mu\text{m}$) observations from the ground for nearby objects ($z \sim 0.01\text{--}0.15$). These lines are relatively strong and have been observed in various studies to measure dust extinction (e.g., Goldader et al. 1995; Veilleux et al. 1999b).

The Pa α /Br γ line ratio predicted by the high-density model is 9.93, deviating from the case B value of 12.1 (Table 6). In the prediction, the Pa α line at the shorter wavelength is weakened relative to the Br γ line at the longer wavelength. This is the same trend as the effect of dust extinction. The Pa α /Br γ line ratio of 9.93 corresponds to dust extinction of $A_V = 6.60$ mag, assuming the case B ratio. This indicates that we cannot distinguish the deviation of the predicted Pa α /Br γ line ratio from that of case B due to the effect of dust extinction. Thus, our model is consistent with the fact that no anomaly has been reported in previous observations of the Pa α /Br γ line ratio.

Among our targets with anomalous Br β /Br α line ratios, the Pa α /Br γ line ratio was observed in IRAS 10494+4424 by Murphy et al. (2001) and in Mrk 273 by Veilleux et al. (1999b). We cannot find observations of the Pa α /Br γ line ratio in IRAS 10565+2448. The Pa α /Br γ line ratio in Mrk 273 is 10.8 ± 1.0 , which is consistent with our prediction. The Pa α /Br γ line ratio in IRAS 10494+4424 was reported to be 16.1 ± 1.5 . This ratio indicates that the Pa α line is enhanced relative to the Br γ line compared to the case B ratio. This is opposite to the effect of dust extinction and also to the devia-

tion of our model from the case B ratio. Thus, the ratio is explained neither by our model nor by the case B ratio with dust extinction. [Murphy et al. \(2001\)](#) regarded this anomaly as not significant. They claimed that the observations of the Pa α and Br γ lines in IRAS 10494+4424 were performed with different apertures, and this made the observed Pa α /Br γ line ratio uncertain by as much as 50%. Thus, we also treat the deviation as not significant here.

Based on the above results, we conclude that our model does not contradict previous observations of the H I line ratios. The deviation of a line intensity ratio from case B due to the high density condition is hardly detectable in ratios other than Br β /Br α , in the optical and near-infrared wavelength regions.

6. STRUCTURE OF HIGH-DENSITY H II REGIONS

We find that we can explain the high Br β /Br α line ratio with the optical-depth effect. In order to make the Br α line optically thick, high-density H II regions are required in our Cloudy model. Herein, we discuss possible structures of such high-density H II regions in ULIRGs.

6.1. Two Extreme Cases

To explain the observed luminosity of the Br α line, we consider two extreme cases for the line-emitting regions: (1) an ensemble of H II regions, each ionized by a single star and (2) a giant H II region where all the ionizing stars are concentrated at the center. For each case, we discuss whether the optical-depth effect can produce high Br β /Br α line ratios.

6.1.1. Ensemble of H II Regions

We here consider an ensemble of H II regions, each of which is represented by the high-density model. In Table 7, we list the observed luminosity of the Br α line for each of the three galaxies with a high Br β /Br α line ratio. In the high-density model, the luminosity of the Br α line produced by a single H II region is found to be $L_{\text{Br}\alpha}^{\text{Model}} = 2.79 \times 10^{36} \text{ erg s}^{-1}$ (Table 5), and we estimate the number of H II regions k_{tot} , as shown in Table 7. From this result, we conclude that $\sim 10^5$ H II regions with high-density conditions are required to explain our observations.

We next estimate the expected number of H II regions along the line of sight, k_{los} , to determine the effect of optical depth on the line emitted from a single H II region and intercepted by other H II regions. We assume a volume filling factor $\varepsilon \sim 10^{-6}$, which is a typical value for H II regions observed in starburst galaxies ([Anantharamaiah et al. 1993](#)). We also assume that H II regions are

Table 7. Comparison of Luminosity with High-Density Model

Object	$L_{\text{Br}\alpha}$	k_{tot}^a
Name	($10^{41} \text{ erg s}^{-1}$)	(10^4)
IRAS 10494+4424	2.31 ± 0.18	8.8
IRAS 10565+2448	1.50 ± 0.09	5.7
Mrk 273	1.58 ± 0.04	6.0

^aThe number of H II regions represented by the high-density model that are required to yield the observed luminosity of the Br α line.

uniformly and spherically distributed. Using the radius R of individual H II regions, the volume of the entire space in which they are distributed as an ensemble can be written as $k_{\text{tot}}R^3/\varepsilon$. Then, the diameter d of that space becomes

$$d \sim (k_{\text{tot}}/\varepsilon)^{1/3}R. \quad (14)$$

On the other hand, k_{los} , the number of H II regions that exist on the diameter, satisfies

$$k_{\text{los}}R^3 \sim \varepsilon dR^2. \quad (15)$$

By comparing Equations (14) and (15), we find

$$k_{\text{los}} \sim k_{\text{tot}}^{1/3} \varepsilon^{2/3}. \quad (16)$$

Substituting $k_{\text{tot}} = 10^5$ and $\varepsilon = 10^{-6}$ into Equation (16), we obtain $k_{\text{los}} \sim 10^{-7/3}$. We assume the relative velocities of H II regions to be of the order of $\sim 100 \text{ km s}^{-1}$, which is a typical line velocity observed in galaxies (e.g., [Osterbrock & Ferland 2006](#)) and is an order of magnitude higher than the thermal velocity. Then, the optical depth of the Br α line caused by the intercepting H II regions is found to be three orders of magnitude smaller than that of the H II region from which the line originates. Thus, we conclude that the line ratio produced in a single H II region is not affected by other H II regions, even if we consider an ensemble of $\sim 10^5$ H II regions.

We therefore conclude that an ensemble of H II regions, in each of which the Br α line is optically thick, can explain the high Br β /Br α line ratio. This ratio is produced within each H II region, and what we observe is a collection of such H II regions. To achieve a column density large enough to make the Br α line optically thick within a single H II region, the gas density must be as high as $n \sim 10^8 \text{ cm}^{-3}$.

6.1.2. Single Giant H II Region

We next consider another simplified model, in which the line-emitting region is not a collection of H II regions but a single giant H II region, where all the ionizing stars are concentrated at the center of a uniform gas. We investigate whether a high $\text{Br}\beta/\text{Br}\alpha$ line ratio can be produced within such a giant H II region by the optical-depth effect.

We have shown that ionizing sources with $Q(\text{H})$ of the order of $\sim 10^{55} \text{ s}^{-1}$ are required to explain the observed luminosity of the $\text{Br}\alpha$ line. Thus, we also assume a central ionizing source of $Q(\text{H}) = 10^{55} \text{ s}^{-1}$, which corresponds to $10^5\text{--}10^6$ OB stars. For the turbulence velocity within the giant H II region, we assume $v_{\text{Turb}} = 100 \text{ km s}^{-1}$. In this case, Equation (8) indicates that $N_4 \sim 2 \times 10^{12} \text{ cm}^{-2}$ is required to make the $\text{Br}\alpha$ line optically thick. Substituting $N_4 = 2 \times 10^{12} \text{ cm}^{-2}$ and $Q(\text{H}) = 10^{55} \text{ s}^{-1}$ into Equation (13), we obtain $n \sim 2 \times 10^7 \text{ cm}^{-3}$ for the gas density required to make the $\text{Br}\alpha$ line optically thick within the giant H II region.

To investigate the $\text{Br}\beta/\text{Br}\alpha$ line ratio quantitatively for this case, we again used the Cloudy code to simulate the giant H II region. Most of the parameters are the same as those tabulated in Table 4, except that $Q(\text{H})$ is now fixed at 10^{55} s^{-1} , n is varied at intervals of 0.5 dex up to $n = 10^{8.5} \text{ cm}^{-3}$, and $v_{\text{Turb}} = 100 \text{ km s}^{-1}$ is adopted. We show the Cloudy results in Figure 12. The observed $\text{Br}\beta/\text{Br}\alpha$ line ratio can be explained if the gas density is within the range $n = 10^{7.5}\text{--}10^{8.0} \text{ cm}^{-3}$. The luminosity of the $\text{Br}\alpha$ line in these conditions is $L_{\text{Br}\alpha} \sim 2\text{--}4 \times 10^{41} \text{ erg s}^{-1}$, and we confirm that this agrees well with the observed value. We thus conclude that gas densities as high as $n \sim 10^8 \text{ cm}^{-3}$ are also required to explain the observed $\text{Br}\beta/\text{Br}\alpha$ line ratio in the extreme case in which the line-emitting region is a single giant H II region with a central ionizing source emitting $Q(\text{H}) = 10^{55} \text{ s}^{-1}$.

There is one caveat to the Cloudy results shown in Figure 12. With $Q(\text{H}) = 10^{55} \text{ s}^{-1}$, the column density of electrons within the H II region exceeds $N_e \sim 2 \times 10^{24} \text{ cm}^{-2}$ for conditions with $n \geq 10^8 \text{ cm}^{-3}$ so the H II region becomes Compton thick. The Cloudy code is not designed to simulate Compton-thick regimes (Ferland et al. 1998); therefore, the validity of the result is not guaranteed in those conditions. The process of Thomson scattering does not include any energy transfer. Thus, we expect that the result for the emergent line ratio is still valid even if the H II region becomes Compton thick.

In summary, for both the two extreme cases, we conclude that gas densities as high as $n \sim 10^8 \text{ cm}^{-3}$ are required to achieve a column density of neutral hydrogen large enough to make the $\text{Br}\alpha$ line optically thick.

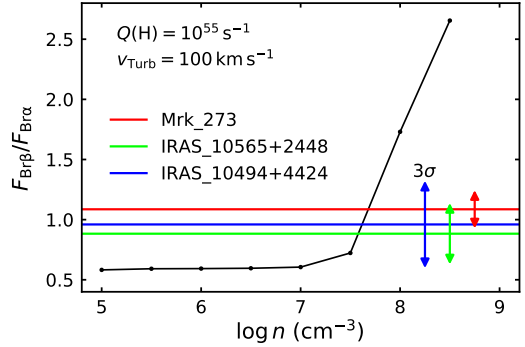


Figure 12. Cloudy results for the $\text{Br}\beta/\text{Br}\alpha$ line ratios for various total hydrogen densities n , with $Q(\text{H}) = 10^{55} \text{ s}^{-1}$ and $v_{\text{Turb}} = 100 \text{ km s}^{-1}$. The horizontal red, green, and blue lines show the observed $F_{\text{Br}\beta}/F_{\text{Br}\alpha}$ ratios for Mrk 273, IRAS 10565+2448, and IRAS 10494+4424, respectively. The range of 3σ uncertainty is shown by the vertical arrows.

We propose this high-density scenario as the most plausible cause of the high $\text{Br}\beta/\text{Br}\alpha$ line ratio.

6.2. Impact of dust grains

The density of $n \sim 10^8 \text{ cm}^{-3}$ is in a regime denser than the densest ultracompact H II regions in our Galaxy (e.g., Kurtz 2000; Churchwell 2002). In this regime, dust can compete with H I for ionization photons. Then, the effective $Q(\text{H})$ for H I is reduced, and a higher number density may be needed to achieve a column density sufficient to make the $\text{Br}\alpha$ line optically thick (Equation (13)). On the other hand, it is also expected that the higher the density, the more the dust is thermally coupled with gas, and the abundance of the dust decreases due to sublimation. The overall influence of the dust includes both of these effects. Because the above Cloudy models are assumed to be dust-free, we here quantitatively evaluate how the results change when the dust is taken into account by modifying the cloudy models.

We start with the case of an ensemble of H II regions. Cloudy simulations were performed with dust. The abundances were changed from the default to a predefined set of the interstellar medium. Both silicate and graphite grains are included with ten size bins for each. The option to treat the dust sublimation was turned on so that the abundance of each grain species steeply decreases when its temperature is above the sublimation temperature. The $\text{Br}\beta/\text{Br}\alpha$ line ratio was calculated as a function of n . To examine the case of the intensest ionization, $Q(\text{H})$ was fixed at 10^{50} s^{-1} (corresponding to an O3 star). Other parameters are the same as in Table 4. The results are shown in Figure 13. With the same parameters as the reference model in the dust-free case ($n = 10^8 \text{ cm}^{-3}$, $Q(\text{H}) = 10^{50} \text{ s}^{-1}$), the $\text{Br}\beta/\text{Br}\alpha$

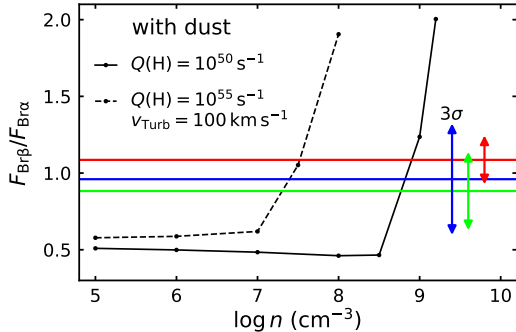


Figure 13. Cloudy results for the $\text{Br}\beta/\text{Br}\alpha$ line ratio obtained when dust grains are included in the simulation. The ratio is calculated as a function of total hydrogen densities n . The black solid line shows the result at $Q(\text{H}) = 10^{50} \text{ s}^{-1}$, which corresponds to the case of an ensemble of H II regions (§6.1.1). The black dashed line shows the result at $Q(\text{H}) = 10^{55} \text{ s}^{-1}$ with $v_{\text{Turb}} = 100 \text{ km s}^{-1}$, which corresponds to the case of a single giant H II region (§6.1.2). The horizontal red, green, and blue lines show the observed $F_{\text{Br}\beta}/F_{\text{Br}\alpha}$ ratios for Mrk 273, IRAS 10565+2448, and IRAS 10494+4424, respectively. The range of 3σ uncertainty is shown by the vertical arrows.

ratio is lowered from 0.94 to 0.46. This is due to the fact that the column density N is not much increased and $\text{Br}\alpha$ does not become optically thick because ionizing photons are consumed by dust, and that the ratio is affected by dust extinction. The ratio of ~ 1 as observed is found at $n = 10^9 \text{ cm}^{-3}$. At this point, $L_{\text{Br}\alpha}^{\text{Model}}$ becomes $2.4 \times 10^{35} \text{ erg s}^{-1}$, which is a factor of 12 lower than in the dust-free reference model. Thus, the estimate of k_{tot} increases up to 10^6 . The estimate of k_{los} changes by only a factor of two, and the possibility that multiple H II regions are aligned along the line of sight and the line emission from the H II region behind is blocked is still negligible.

Next, we move on to the case of a single giant H II region. In the above case of the H II region ensemble with dust, k_{tot} has increased by one order of magnitude. However, in this case, the $Q(\text{H})$ needed is expected to be the same as in the dust-free model, $Q(\text{H}) = 10^{55} \text{ s}^{-1}$. This is because if multiple stars are concentrated near the center, they will destroy dust grains in the same region together, and thus cancel out the dust effect more efficiently than in the ensemble case, where each star destroys the surrounding dust on its own. We thus changed the $Q(\text{H})$ of the above Cloudy model with dust to 10^{55} s^{-1} and calculated the $\text{Br}\beta/\text{Br}\alpha$ ratio as a function of n . The specification of $v_{\text{Turb}} = 100 \text{ km s}^{-1}$ was also added. The results are shown in Figure 13. A ratio of ~ 1 is found at $n = 10^{7.5} \text{ cm}^{-3}$. Therefore, a high-density situation is still necessary. At this point,

$L_{\text{Br}\alpha}^{\text{Model}} = 1 \times 10^{42} \text{ erg s}^{-1}$, which fully explains the observed line luminosities (Table 7). Hence, as predicted, in the case of a giant H II region, the observation results can be explained by $Q(\text{H}) = 10^{55} \text{ s}^{-1}$ ($\sim 10^5$ O3 stars) even if dust is taken into consideration.

The actual situation is expected to be bracketed between these two extreme cases. Therefore, we conclude that the number of massive stars needed to explain the $\text{Br}\beta/\text{Br}\alpha$ anomaly may be increased by up to an order of magnitude from the estimates based on the assumption of the dust-free gas. The main conclusion (the high density gas is needed to explain the anomalous H I line ratio) is the same for the cases even with dust.

6.3. Comparison of Lifetime with Galactic Ultracompact H II Regions

In the dust-free ensemble model, about 10^5 H II regions with gas at high densities $n \sim 10^8 \text{ cm}^{-3}$ are required to explain the high $\text{Br}\beta/\text{Br}\alpha$ line ratios. Herein, we discuss the possibility of observing so many high-density H II regions in ULIRGs by comparison with the ultracompact H II regions in our Galaxy.

Ultracompact H II regions in our Galaxy (e.g., Kurtz 2000; Churchwell 2002) are reported to contain high-density gas up to $n \sim 10^7 \text{ cm}^{-3}$ and to have sizes of the order of 10^{-2} pc (e.g., de Pree et al. 1995). The densities and sizes of these ultracompact H II regions are comparable to those of the high-density H II regions required in our model. We thus consider the high-density H II regions in our model as analogous to the ultracompact H II regions in our Galaxy.

A simple estimate of the lifetime of an H II region in an ultracompact state with a size $r \sim 10^{-2} \text{ pc}$ can be obtained by dividing r by the sound speed v_s in the ionized material ($v_s \sim 10 \text{ km s}^{-1}$ at $T = 10000 \text{ K}$), assuming that the H II region expands at a speed comparable to v_s . This yields a lifetime $r/v_s \sim 10^3 \text{ yr}$ for an ultracompact H II region in our Galaxy. Another estimate can be obtained from the number of ultracompact H II regions, which is estimated to be $\sim 10^3$ in our Galaxy (Churchwell 2002). Adopting the formation rate of O stars to be $\sim 10^{-2} \text{ stars yr}^{-1}$ in our Galaxy (de Pree et al. 1995), we get instead for the lifetime of an ultracompact H II region $\sim 10^5$, some two orders of magnitude longer than that obtained from the simple expansion of an H II region. This large difference between the estimated lifetimes is recognized as the ‘‘lifetime problem,’’ first mentioned by Wood & Churchwell (1989), which still remains an open question (e.g., Kurtz 2000; Churchwell 2002). Herein, we simply adopt $\sim 10^5 \text{ yr}$ as the representative lifetime of an ultracompact H II region.

We assume that the high-density H II regions required in our high-density model have a lifetime of the same order ($\sim 10^5$ yr) as those of the ultracompact H II regions in our Galaxy. We note that the star formation rate (SFR) in a ULIRG is about two orders of magnitude higher than that in our Galaxy (Sanders et al. 1988). Scaling the number of the ultracompact H II regions observed in our Galaxy ($\sim 10^3$; Churchwell 2002) with the SFR, we thus expect the number of high-density H II regions to be on the order of $\sim 10^5$ in a ULIRG. Thus, we conclude that it is indeed possible to have $\sim 10^5$ high-density H II regions in a ULIRG, as our model predicts.

After the $\sim 10^5$ yr lifetime of the ultracompact phase, the gas density of an H II region is expected to fall below $\sim 10^7$ cm $^{-3}$ as the H II region expands (de Pree et al. 1995). The typical lifetime of an O star is on the order of 10^6 yr (Osterbrock & Ferland 2006), which is an order of magnitude longer than that of the ultracompact H II regions. Thus, the number of H II regions with gas densities lower than $\sim 10^7$ cm $^{-3}$ is expected to be an order of magnitude larger than that of the ultracompact H II regions. However, to explain the high Br β /Br α line ratios, our model requires most H II regions to be in the ultracompact phase. Our results thus indicate that some mechanism is required to ensure that the Brackett lines from the H II regions in ULIRGs are dominated by those emitted from ultracompact H II regions. This problem remains when the dust is taken into account, where a larger number of denser H II regions are required if they are isolated from each other.

7. PREDICTION TO RADIO RECOMBINATION LINES

We consider the effect of high densities on radio recombination lines. Our model requires gas densities $n = 10^8$ cm $^{-3}$. At such high densities, collisional processes become important for high- \mathcal{N} states. As shown in Figure 7, hydrogen levels with low principal quantum numbers ($\mathcal{N} \leq 15$) are not dominated by collisions, even at a density $n = 10^8$ cm $^{-3}$. In contrast, the collisional processes start to contribute significantly for states with $\mathcal{N} \geq 20$. This indicates that hydrogen radio recombination lines emitted with transitions involving high- \mathcal{N} states are affected by the high densities our model predicts.

Peters et al. (2012) showed that at a density $n = 10^8$ cm $^{-3}$, $b_{\mathcal{N}} \sim 1$ for levels with $\mathcal{N} > 30$. For $n = 10^6$ cm $^{-3}$, where anomalous Br β /Br α line ratios are not found in the Cloudy simulations, only states with $\mathcal{N} > 50$ become thermalized. This indicates that observations of radio recombination lines with low- \mathcal{N} transitions ($\mathcal{N} < 50$) are required to probe our model

predictions. However, previous observations of radio recombination lines were mainly focused on high- \mathcal{N} transitions because of difficulty of observations at the high frequencies where the transitions with $\mathcal{N} < 50$ are located.

Radio recombination lines involving levels with $\mathcal{N} < 50$ are now observable within the frequency range of ALMA. We thus predict that such radio recombination lines will be found to be thermalized in those galaxies with Br β /Br α line-ratio anomalies, although the radio recombination lines are generally very weak (e.g., Izumi et al. 2016; Michiyama et al. 2020).

8. SUMMARY

We conducted systematic observations of the H I Br α and Br β lines with the AKARI IRC for 52 nearby ($z < 0.3$) ULIRGs. We detected Br α and Br β lines in 33 ULIRGs. Among these, three galaxies, IRAS 10494+4424, IRAS 10565+2448, and Mrk 273, show Br β /Br α line ratios (0.96 ± 0.12 , 0.883 ± 0.085 , and 1.086 ± 0.053 , respectively), which are significantly higher than that for case B (0.565). We also find that ULIRGs have a tendency to exhibit higher Br β /Br α line ratios than those observed in Galactic H II regions. If dust extinction affects the flux of the lines, the Br β /Br α line ratio will decrease below 0.565 because the Br β line has a shorter wavelength and so is more attenuated than the Br α line. Thus, we cannot explain the high Br β /Br α line ratio with a combination of case B theory and dust extinction.

We investigated the cause of this anomaly and obtained the following results:

1. We explored the possibility of contamination of the Brackett lines by other lines. We identified one candidate, the H $_2$ (1,0) O(2) line, with a wavelength of 2.627 μ m, that is close to the wavelength of the Br β line (2.626 μ m). We estimated the flux of the H $_2$ (1,0) O(2) line from that of another molecular hydrogen line, H $_2$ (1,0) O(3) at 2.802 μ m, assuming that the line ratio corresponds to that of a 2000 K shock model (Black & van Dishoeck 1987). The expected flux of the H $_2$ (1,0) O(2) line is 5–12% of that of the observed Br β line. Consequently, the Br β /Br α line ratio is still more than 3σ higher than that for case B in IRAS 10565+2448 and Mrk 273 even after we subtract the flux of the H $_2$ (1,0) O(2) line from that of the Br β line. Thus, we conclude that contamination does not provide a complete explanation of the high Br β /Br α line ratio.

2. For the case in which the Brackett lines are optically thin, we cannot explain the high $\text{Br}\beta/\text{Br}\alpha$ line ratio with any of the three possible excitation mechanisms: recombination, collisional excitation, or resonant excitation.
3. We find that we can explain the deviation of the $\text{Br}\beta/\text{Br}\alpha$ line ratio from that of case B if the $\text{Br}\alpha$ line becomes optically thick while the $\text{Br}\beta$ line is still optically thin.
4. We simulated H II regions, each ionized by a single star, with the Cloudy code and found that the high $\text{Br}\beta/\text{Br}\alpha$ line ratio can be explained when the $\text{Br}\alpha$ line becomes optically thick. To achieve a column density large enough to make the $\text{Br}\alpha$ line optically thick within a single H II region, the gas density must be as high as $n \sim 10^8 \text{ cm}^{-3}$.
5. We investigated the ratios of optical H I lines in the galaxies in our sample that show high $\text{Br}\beta/\text{Br}\alpha$ line ratios. We found that the fluxes of the optical lines are highly affected by dust extinction, and it is difficult to tell whether the line ratio contradicts case B theory. We conclude that the deviation of the H I line ratios from those of case B can be seen clearly only in the infrared H I lines because the optical lines are strongly affected by dust extinction.
6. We investigated the consistency of our high-density model with other infrared H I line observations. We compared the H I line ratios other than $\text{Br}\beta/\text{Br}\alpha$ with those predicted by the high-density model for the three galaxies with high $\text{Br}\beta/\text{Br}\alpha$ line ratios. We conclude that our model is consistent with previous observations of the $\text{Pa}\alpha/\text{Br}\gamma$ line ratio.
7. We consider two extreme cases for the line-emitting regions: (1) an ensemble of H II regions, each ionized by a single star and (2) a giant H II region where all the ionizing stars are concentrated at the center. For both the cases, we conclude that gas densities as high as $n \sim 10^8 \text{ cm}^{-3}$ are required to achieve a column density of neutral

hydrogen large enough to make the $\text{Br}\alpha$ line optically thick. We propose this high-density scenario as the most plausible cause of the high $\text{Br}\beta/\text{Br}\alpha$ line ratio. The required density may be increased by up to an order of magnitude if dust grains are taken into account.

8. Our model requires high-density H II regions with $n = 10^8 \text{ cm}^{-3}$. This affects the high- \mathcal{N} transitions of H I lines, which fall in the radio-frequency range. We predict that radio recombination lines with $\mathcal{N} < 50$ are thermalized in galaxies with high $\text{Br}\beta/\text{Br}\alpha$ line ratios.

ACKNOWLEDGMENTS

We thank the anonymous referee for reading our paper carefully and sending many useful suggestions for improvement. This study is based on the observations made with *AKARI*, a JAXA project, with the participation of ESA. We also thank the Lick Observatory staff for their assistance. This research made use of the NASA/IPAC Extragalactic Database, which is operated by the Jet Propulsion Laboratory, California Institute of Technology, under contract with the National Aeronautics and Space Administration. Data analysis was in part carried out on the Multi-wavelength Data Analysis System operated by the Astronomy Data Center (ADC), National Astronomical Observatory of Japan. This work is supported by JSPS KAKENHI Grant Number 26247030. K.Y. is supported through the Leading Graduates Schools Program, Advanced Leading Graduate Course for Photon Science, by the Ministry of Education, Culture, Sports, Science and Technology of Japan. S.B. is supported by JSPS KAKENHI Grant Number JP19J00892.

Facilities: *AKARI*(IRC), Nickel: 1.0 m

Software: Cloudy (ver. 10.00; Ferland et al. 1998), IRC Spectroscopy Toolkit (Ohyama et al. 2007; Baba et al. 2016), IPython (Perez & Granger 2007), Jupyter Notebook (Kluyver et al. 2016), NumPy (Harris et al. 2020), SciPy (Virtanen et al. 2020), Pandas (McKinney 2010), Matplotlib (Hunter 2007), Astropy (Astropy Collaboration et al. 2013, 2018), Lmfit (Newville et al. 2020)

APPENDIX

A. NULIZ TARGETS

We summarize here the properties of the two *AKARI* targets added from the NULIZ program. The observa-

tion log and basic information are listed in Tables 8 and

Table 8. Observation Log for NULIZ Targets

Object Name	Observation ID	Observation Date
IRAS 09022–3615	3051018.1	2007 May 26
IRAS 10565+2448	3051019.1	2007 May 28

Table 9. Basic Information for NULIZ Targets

Object Name	z^a	D_L^b (Mpc)	F_{25}^c (Jy)	F_{60}^c (Jy)	F_{100}^c (Jy)	L_{IR}^d ($10^{12}L_{\odot}$)	Optical ^e class	Ref. ^f
IRAS 09022–3615	0.060	266	1.20	11.6	11.1	1.64	H II	1
IRAS 10565+2448	0.043	190	1.27	12.1	15.0	1.07	H II	2

^aRedshift.

^bLuminosity distance calculated from z using our adopted cosmology.

^cIRAS fluxes at 25 μm (F_{25}), 60 μm (F_{60}), and 100 μm (F_{100}).

^dTotal infrared (3–1100 μm) luminosity calculated with $L_{\text{IR}} = 4\pi D_L^2(\xi_1\nu F_{25} + \xi_2\nu F_{60} + \xi_3\nu F_{100})$, where $(\xi_1, \xi_2, \xi_3) = (2.403, -0.2454, 1.6381)$ (Dale & Helou 2002).

^eOptical classification of galaxies.

^fReferences for redshifts: (1) Strauss et al. (1992); (2) Downes et al. (1993).

Table 10. Flux Ratios of the H α and H β Lines

Object Name	$F_{\text{H}\beta}/F_{\text{H}\alpha}$	$A_V^{\text{opt } a}$ (mag)	Reference ^b
IRAS 09022–3615	0.18 \pm 0.009	1.90 \pm 0.14	1
IRAS 10565+2448	0.06 \pm 0.003	4.83 \pm 0.14	2

^aVisual extinction derived from H α /H β line ratio.

^bReferences for optical line ratio: (1) Lee et al. (2011); (2) Veilleux et al. (1995).

9. The H β /H α line ratio used in §5.2 is summarized in Table 10.

B. LINE RATIO IN THE GALACTIC H II REGIONS

Our results for the high Br β /Br α line ratio indicate that conditions in the H II regions in the ULIRGs that exhibit the anomalies are different from those of Galactic H II regions, where the case B theory explains the line ratios well. To investigate the difference, we here discuss the applicability of the case B line ratio for the Br α and Br β lines in Galactic H II regions.

Because of the difficulty of observing the wavelength range where the Br α and Br β lines lie due to the atmospheric absorption, previous observations have been limited to those conducted in space, namely, observations with the *ISO* and *AKARI* satellites. Accordingly, we investigated observations of Galactic H II regions obtained with these two satellites.

B.1. *ISO* Observations

Lutz et al. (1996) obtained a 2.4–45 μm spectrum of the Galactic center with the Short Wavelength Spectrometer on board *ISO*. The 14'' \times 21'' aperture was

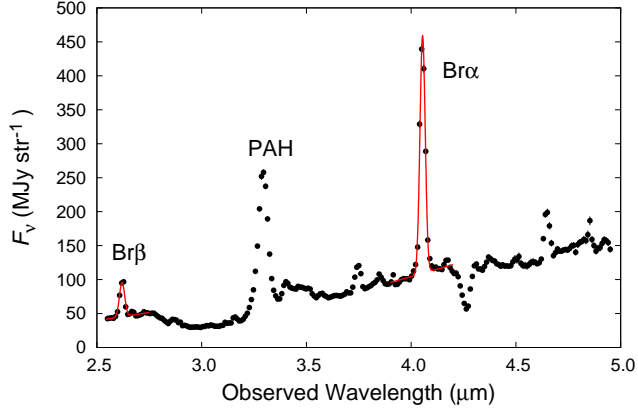


Figure 14. Typical example of a cataloged spectrum of a Galactic H II region by Mori et al. (2014). The spectrum was obtained from the position -04 of W31a (ID: 5200165.1) using the “Nh” slit. The best-fit Gaussian profile for the Br α and Br β lines are shown as red curves.

centered on Sgr A* to cover H II regions in the Galactic center region. They detected H I lines, including the Br α and Br β lines, in the wavelength range 2.5–9.0 μm . The Br β /Br α line ratio at the Galactic center was reported to be ~ 0.25 , which is consistent with case B plus dust extinction (Lutz 1999). Lutz (1999) also discussed the applicability of case B in the Galactic center using the Br α line, the Pf α line ($\mathcal{N} = 6 \rightarrow 5$; 7.46 μm), and a blend of the Hu β line ($\mathcal{N} = 8 \rightarrow 6$; 7.50 μm) with the $\mathcal{N} = 11 \rightarrow 7$ transition (7.51 μm). They concluded that the flux ratios of these lines were consistent with the case B line ratios and that the population of the respective upper levels followed case B. Thus, the *ISO* results indicate that the case B line ratio is applicable to H II regions near the Galactic center.

B.2. AKARI Observations

Using *AKARI* near-infrared spectroscopy, Mori et al. (2014) conducted a systematic observation of 36 Galactic H II regions and provided a catalog of 2.5–5.0 μm spectra of such objects.² A typical example from the cataloged spectra is shown in Figure 14.

We determined the Br α and Br β line fluxes for those Galactic H II regions using the 232 cataloged spectra. We fitted the Br α and Br β lines separately, with a Gaussian profile and a linear continuum for each spectrum. Following Mori et al. (2014), we fixed the FWHM of the Gaussian profile at 0.031 μm for spectra taken with the “Ns” slit and 0.025 μm for those taken with “Nh” slit in order to match the spectral resolution of the slits.

² The catalog is publicly available at URL: http://www.ir.isas.jaxa.jp/AKARI/Archive/Catalogues/IRC_GALHILspec/

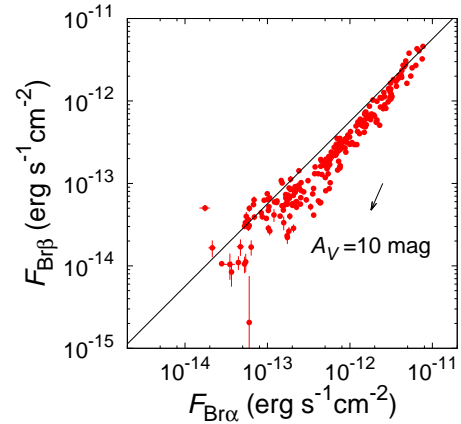


Figure 15. The fluxes of the Br α and Br β lines for Galactic H II regions obtained from the spectral catalog of Mori et al. (2014). The solid line shows the theoretical line ratio for case B: $F_{\text{Br}\beta}/F_{\text{Br}\alpha} = 0.565$. The extinction vector corresponding to $A_V = 10$ mag is shown as the black arrow.

The central wavelengths of the lines were also fixed at 4.05 μm for the Br α line and at 2.63 μm for the Br β line. The range of wavelengths used for the fitting was ± 0.15 μm around the central wavelength of each line. We then determined the line flux by integrating the best-fit Gaussian profile. A typical example of the Gaussian fitting is shown in Figure 14.

We show the fluxes of the Br α and Br β lines obtained for the Galactic H II regions in Figure 15. The results show that almost all the Br β /Br α line ratios are lower than that for case B, except for a few spectra. This indicates that the Br β /Br α line ratios of Galactic H II regions can be explained by case B condition plus dust extinction, which is typically $A_V \sim 10$ mag.

Combining the results of the *ISO* and *AKARI* observations, we conclude that the case B condition is valid for Galactic H II regions. Thus, the anomalous Br β /Br α line ratios found in some ULIRGs indicate that conditions in the H II regions in those ULIRGs differ from the case B conditions.

C. DETAILED DISCUSSIONS ON RESONANT PROCESSES

This appendix provides detailed discussions about the effect of resonant excitations on the Br β /Br α line ratio. First, we discuss the $\mathcal{N} = 1 \rightarrow 6$ resonance referred in §4.2. Then, we consider the $\mathcal{N} = 1 \rightarrow 4$ resonance mentioned in §4.3.2.

C.1. Resonant Excitation to the $\mathcal{N} = 6$ State

With resonant excitation, the hydrogen $\mathcal{N} = 6$ state is enhanced if a strong line with a wavelength comparable to that of the transition $\mathcal{N} = 6 \rightarrow 1$ (937.8 Å) exists.

We denote this (unknown) line by X_6 and discuss its effect on the $\text{Br}\beta/\text{Br}\alpha$ line ratio in the optically thin case described in §4.2.

First, we assume a case in which hydrogen is excited solely by this resonant excitation. Let x_6 be the number of resonance excitations per unit volume and unit time ($\text{cm}^{-3} \text{s}^{-1}$). Then, the number of $\text{Br}\beta$ transitions ($\mathcal{N} = 6 \rightarrow 4$) caused by the resonant excitation can be written as $x_6 A_{6,4}/A_6 \sim 0.22x_6$, and the number of $\text{Br}\alpha$ transitions ($\mathcal{N} = 5 \rightarrow 4$) is given by $x_6 C_{6,5} C_{5,4} = 0.11x_6$. Here, the A and C symbols are the Einstein A coefficient and cascade matrix introduced in §4.1.1, respectively. The $\text{Br}\beta/\text{Br}\alpha$ line ratio is thus found to be $F_{\text{Br}\beta}/F_{\text{Br}\alpha} = 0.22x_6 h\nu_{\text{Br}\beta}/0.11x_6 h\nu_{\text{Br}\alpha} \sim 3.2$. Therefore, it is possible for resonant excitation to make the line ratio consistent with our observations, given the existence of an appropriate line transition X_6 .

Next we discuss how strong the X_6 line must be in order to explain the observed anomaly. Taking the resonant excitation rate x_6 into account in Equation (2), we now write the level populations for $\mathcal{N} = 5$ and 6 as

$$\begin{aligned} n'_6 A_6 &= n_p n_e \sum_{\mathcal{N}'=6}^{\infty} \alpha_{\mathcal{N}'} C_{\mathcal{N}',6} + x_6, \\ \therefore n'_6 &= n_p n_e \frac{\sum_{\mathcal{N}'=6}^{\infty} \alpha_{\mathcal{N}'} C_{\mathcal{N}',6}}{A_6} + \frac{x_6}{A_6}, \end{aligned} \quad (\text{C1})$$

and

$$\begin{aligned} n'_5 A_5 &= n_p n_e \sum_{\mathcal{N}'=6}^{\infty} \alpha_{\mathcal{N}'} C_{\mathcal{N}',5} + C_{6,5} x_6, \\ \therefore n'_5 &= n_p n_e \frac{\sum_{\mathcal{N}'=5}^{\infty} \alpha_{\mathcal{N}'} C_{\mathcal{N}',5}}{A_5} + \frac{C_{6,5} x_6}{A_5}. \end{aligned} \quad (\text{C2})$$

In order to explain the observed anomaly, in which $F_{\text{Br}\beta}/F_{\text{Br}\alpha} \sim 1$, we require the ratio of the level populations to be $n'_6/n'_5 \sim 2.27$. Using Equations (C1) and (C2), we find

$$\begin{aligned} & n_p n_e \frac{\sum_{\mathcal{N}'=6}^{\infty} \alpha_{\mathcal{N}'} C_{\mathcal{N}',6}}{A_6} + \frac{x_6}{A_6} \\ &= 2.27 \left(n_p n_e \frac{\sum_{\mathcal{N}'=5}^{\infty} \alpha_{\mathcal{N}'} C_{\mathcal{N}',5}}{A_5} + \frac{C_{6,5} x_6}{A_5} \right), \\ \therefore x_6 &= 2.29 \times 10^{-14} \left(\frac{n}{\text{cm}^{-3}} \right)^2 \text{cm}^{-3} \text{s}^{-1}, \end{aligned} \quad (\text{C3})$$

where we have approximated $n_e n_p \sim n^2$. Assuming that all photons emitted in the X_6 line are absorbed by the hydrogen atoms, we can obtain that x_6 is equal to the emission rate of the X_6 line. We write this rate as $n \xi_X f_{X_6} A_{X_6}$, where ξ_X is the abundance of the atoms emitting the X_6 line, relative to hydrogen; f_{X_6} is the

fraction of excited atoms that can radiate the X_6 line, relative to those in other states; and A_{X_6} is the Einstein A coefficient for the X_6 line. From Equation (C3), we thus obtain

$$A_{X_6} = 2.29 \times 10^{-14} f_{X_6}^{-1} \xi_X^{-1} \left(\frac{n}{\text{cm}^{-3}} \right) \text{s}^{-1}. \quad (\text{C4})$$

It is difficult to estimate the fraction f_{X_6} , so we here assume the most extreme case that it is of order unity in order to take weak lines into consideration. At a gas density $n = 10^3 \text{cm}^{-3}$ and assuming that the atoms emitting the X_6 line have an abundance similar to those of the metals, $\xi_X \sim 10^{-4}$, we find A_{X_6} to be $\sim 10^{-7} \text{s}^{-1}$, which is close to the values for forbidden lines. This indicates that if a line exists with a wavelength $\sim 937.8 \text{\AA}$ and a transition probability comparable to those of forbidden lines, then the resonant process would be able to make the $\text{Br}\beta/\text{Br}\alpha$ line ratio anomalously high.

C.2. Resonant Excitation to the $\mathcal{N} = 4$ State

Herein, we discuss the effect of the $\mathcal{N} = 1 \rightarrow 4$ resonant excitation on the $\text{Br}\beta/\text{Br}\alpha$ line ratio in the optically thick case described in §4.3.2. We denote the possible resonant line by X_4 and write the rate of resonant excitation by this line as x_4 ($\text{cm}^{-3} \text{s}^{-1}$). From Equation (2), the $\mathcal{N} = 4$ state is populated by the recombination process at the rate $n_e n_p \sum_{\mathcal{N}'=4}^{\infty} \alpha_{\mathcal{N}'} C_{\mathcal{N}',4} \sim 6.2 \times 10^2 \text{cm}^{-3} \text{s}^{-1}$ at $n = 10^8 \text{cm}^{-3}$. This indicates that if x_4 is larger than $\sim 10^3 \text{cm}^{-3} \text{s}^{-1}$, the resonant process can significantly populate the $\mathcal{N} = 4$ state when $n = 10^8 \text{cm}^{-3}$.

In the same way as for the hypothetical $\mathcal{N} = 1 \rightarrow 6$ resonance we discussed in §C.1, we can estimate the transition probability A_{X_4} of the X_4 line that is required to make the resonant process dominant for the $\mathcal{N} = 4$ population. We assume that all photons emitted by the X_4 line are absorbed by hydrogen such that x_4 is equal to the rate of emission of the X_4 line, $n \xi_X f_{X_4} A_{X_4}$, where ξ_X is the abundance of the atoms emitting the X_4 line relative to hydrogen, and f_{X_4} is the fraction of excited atoms which can radiate the X_4 line relative to those in other states. We assume f_{X_4} to be of the order of unity as the most extreme case. At a gas density of $n = 10^8 \text{cm}^{-3}$ and assuming that the atoms emitting the X_4 line have an abundance similar to those of the metals, i.e., $\xi_X \sim 10^{-4}$, we estimate A_{X_4} to be $\sim 10^{-1} \text{s}^{-1}$. Thus, if a line with a wavelength of $\sim 972.5 \text{\AA}$ and a transition probability of $\sim 10^{-1} \text{s}^{-1}$ exists, we should take the resonant process into consideration in determining the population of the $\mathcal{N} = 4$ state.

REFERENCES

- Ahn, C. P., Alexandroff, R., Allende Prieto, C., et al. 2012, *ApJS*, 203, 21, doi: [10.1088/0067-0049/203/2/21](https://doi.org/10.1088/0067-0049/203/2/21)
- Anantharamaiah, K. R., Zhao, J.-H., Goss, W. M., & Viallefond, F. 1993, *ApJ*, 419, 585, doi: [10.1086/173510](https://doi.org/10.1086/173510)
- Arthur, S. J., Medina, S. N. X., & Henney, W. J. 2016, *MNRAS*, 463, 2864, doi: [10.1093/mnras/stw2165](https://doi.org/10.1093/mnras/stw2165)
- Astropy Collaboration, Robitaille, T. P., Tollerud, E. J., et al. 2013, *A&A*, 558, A33, doi: [10.1051/0004-6361/201322068](https://doi.org/10.1051/0004-6361/201322068)
- Astropy Collaboration, Price-Whelan, A. M., Sipőcz, B. M., et al. 2018, *AJ*, 156, 123, doi: [10.3847/1538-3881/aabc4f](https://doi.org/10.3847/1538-3881/aabc4f)
- Baba, S., Nakagawa, T., Shirahata, M., et al. 2016, *PASJ*, 68, 27, doi: [10.1093/pasj/psw013](https://doi.org/10.1093/pasj/psw013)
- Black, J. H., & van Dishoeck, E. F. 1987, *ApJ*, 322, 412, doi: [10.1086/165740](https://doi.org/10.1086/165740)
- Churchwell, E. 2002, *ARA&A*, 40, 27, doi: [10.1146/annurev.astro.40.060401.093845](https://doi.org/10.1146/annurev.astro.40.060401.093845)
- Cox, A. N., ed. 2000, *Allen's astrophysical quantities*, 4th edn. (New York: AIP Press; Springer)
- Dale, D. A., & Helou, G. 2002, *ApJ*, 576, 159, doi: [10.1086/341632](https://doi.org/10.1086/341632)
- de Pree, C. G., Rodriguez, L. F., & Goss, W. M. 1995, *RMxAA*, 31, 39
- Downes, D., Solomon, P. M., & Radford, S. J. E. 1993, *ApJL*, 414, L13, doi: [10.1086/186984](https://doi.org/10.1086/186984)
- Draine, B. T. 2003, *ARA&A*, 41, 241, doi: [10.1146/annurev.astro.41.011802.094840](https://doi.org/10.1146/annurev.astro.41.011802.094840)
- Ferland, G. J., Korista, K. T., Verner, D. A., et al. 1998, *PASP*, 110, 761, doi: [10.1086/316190](https://doi.org/10.1086/316190)
- Genzel, R., Lutz, D., Sturm, E., et al. 1998, *ApJ*, 498, 579, doi: [10.1086/305576](https://doi.org/10.1086/305576)
- Glass, I. S. 1999, *Handbook of Infrared Astronomy* (Cambridge, New York: Cambridge University Press)
- Goldader, J. D., Joseph, R. D., Doyon, R., & Sanders, D. B. 1995, *ApJ*, 444, 97, doi: [10.1086/175585](https://doi.org/10.1086/175585)
- . 1997, *ApJ*, 474, 104, doi: [10.1086/303448](https://doi.org/10.1086/303448)
- Harris, C. R., Millman, K. J., van der Walt, S. J., et al. 2020, *Nature*, 585, 357, doi: [10.1038/s41586-020-2649-2](https://doi.org/10.1038/s41586-020-2649-2)
- Hummer, D. G., & Storey, P. J. 1987, *MNRAS*, 224, 801, doi: [10.1093/mnras/224.3.801](https://doi.org/10.1093/mnras/224.3.801)
- Hunter, J. D. 2007, *Computing in Science and Engineering*, 9, 90, doi: [10.1109/MCSE.2007.55](https://doi.org/10.1109/MCSE.2007.55)
- Imanishi, M., Nakagawa, T., Ohyama, Y., et al. 2008, *PASJ*, 60, S489, doi: [10.1093/pasj/60.sp2.S489](https://doi.org/10.1093/pasj/60.sp2.S489)
- Izumi, T., Nakanishi, K., Imanishi, M., & Kohno, K. 2016, *MNRAS*, 459, 3629, doi: [10.1093/mnras/stw324](https://doi.org/10.1093/mnras/stw324)
- Johnson, L. C. 1972, *ApJ*, 174, 227, doi: [10.1086/151486](https://doi.org/10.1086/151486)
- Kennicutt, Robert C., J. 1998, *ARA&A*, 36, 189, doi: [10.1146/annurev.astro.36.1.189](https://doi.org/10.1146/annurev.astro.36.1.189)
- Kim, D. C., Veilleux, S., & Sanders, D. B. 1998, *ApJ*, 508, 627, doi: [10.1086/306409](https://doi.org/10.1086/306409)
- Kluyver, T., Ragan-Kelley, B., Pérez, F., et al. 2016, in *Positioning and Power in Academic Publishing: Players, Agents and Agendas*, ed. L. Loizides & B. Schmidt (IOP Press), 87–90, doi: [10.3233/978-1-61499-649-1-87](https://doi.org/10.3233/978-1-61499-649-1-87)
- Komatsu, E., Smith, K. M., Dunkley, J., et al. 2011, *ApJS*, 192, 18, doi: [10.1088/0067-0049/192/2/18](https://doi.org/10.1088/0067-0049/192/2/18)
- Kurtz, S. E. 2000, in *Revista Mexicana de Astronomía y Astrofísica Conference Series*, Vol. 9, *Revista Mexicana de Astronomía y Astrofísica Conference Series*, ed. S. J. Arthur, N. S. Brickhouse, & J. Franco, 169–176
- Lee, J. C., Hwang, H. S., Lee, M. G., Kim, M., & Kim, S. C. 2011, *MNRAS*, 414, 702, doi: [10.1111/j.1365-2966.2011.18437.x](https://doi.org/10.1111/j.1365-2966.2011.18437.x)
- Lee, J. C., Hwang, H. S., Lee, M. G., Kim, M., & Lee, J. H. 2012, *ApJ*, 756, 95, doi: [10.1088/0004-637X/756/1/95](https://doi.org/10.1088/0004-637X/756/1/95)
- Lorente, R., Onaka, T., Yoshifusa, I., et al. 2008, *AKARI IRC Data User Manual (Version 1.4)*. <https://www.ir.isas.jaxa.jp/AKARI/Observation/support/IRC/>
- Lutz, D. 1999, in *ESA Special Publication*, Vol. 427, *The Universe as Seen by ISO*, ed. P. Cox & M. Kessler, 623
- Lutz, D., Feuchtgruber, H., Genzel, R., et al. 1996, *A&A*, 315, L269
- McKinney, W. 2010, in *Proc. 9th Python in Science Conf.*, ed. S. van der Walt & J. Millman, Vol. 445, 51–56
- Michiyama, T., Iono, D., Nakanishi, K., et al. 2020, *ApJ*, 895, 85, doi: [10.3847/1538-4357/ab88a5](https://doi.org/10.3847/1538-4357/ab88a5)
- Mori, T. I., Onaka, T., Sakon, I., et al. 2014, *ApJ*, 784, 53, doi: [10.1088/0004-637X/784/1/53](https://doi.org/10.1088/0004-637X/784/1/53)
- Murakami, H., Baba, H., Barthel, P., et al. 2007, *PASJ*, 59, S369, doi: [10.1093/pasj/59.sp2.S369](https://doi.org/10.1093/pasj/59.sp2.S369)
- Murphy, T. W., J., Soifer, B. T., Matthews, K., Armus, L., & Kiger, J. R. 2001, *AJ*, 121, 97, doi: [10.1086/318031](https://doi.org/10.1086/318031)
- Newville, M., Otten, R., Nelson, A., et al. 2020, *lmfit/lmfit-py 1.0.1*, 1.0.1, Zenodo, doi: [10.5281/zenodo.3814709](https://doi.org/10.5281/zenodo.3814709)
- Ohya, Y., Onaka, T., Matsuhara, H., et al. 2007, *PASJ*, 59, S411, doi: [10.1093/pasj/59.sp2.S411](https://doi.org/10.1093/pasj/59.sp2.S411)
- Onaka, T., Matsuhara, H., Wada, T., et al. 2007, *PASJ*, 59, S401, doi: [10.1093/pasj/59.sp2.S401](https://doi.org/10.1093/pasj/59.sp2.S401)
- Osterbrock, D. E., & Ferland, G. J. 2006, *Astrophysics of gaseous nebulae and active galactic nuclei*, 2nd edn. (Sausalito, CA: University Science Books)
- Perez, F., & Granger, B. E. 2007, *Computing in Science and Engineering*, 9, 21, doi: [10.1109/MCSE.2007.53](https://doi.org/10.1109/MCSE.2007.53)
- Peters, T., Longmore, S. N., & Dullemond, C. P. 2012, *MNRAS*, 425, 2352, doi: [10.1111/j.1365-2966.2012.21676.x](https://doi.org/10.1111/j.1365-2966.2012.21676.x)

- Sanders, D. B., & Mirabel, I. F. 1996, *ARA&A*, 34, 749, doi: [10.1146/annurev.astro.34.1.749](https://doi.org/10.1146/annurev.astro.34.1.749)
- Sanders, D. B., Soifer, B. T., Elias, J. H., et al. 1988, *ApJ*, 325, 74, doi: [10.1086/165983](https://doi.org/10.1086/165983)
- Seaton, M. J. 1959, *MNRAS*, 119, 90, doi: [10.1093/mnras/119.2.90](https://doi.org/10.1093/mnras/119.2.90)
- Shih, H.-Y., & Rupke, D. S. N. 2010, *ApJ*, 724, 1430, doi: [10.1088/0004-637X/724/2/1430](https://doi.org/10.1088/0004-637X/724/2/1430)
- Storey, P. J., & Hummer, D. G. 1995, *MNRAS*, 272, 41, doi: [10.1093/mnras/272.1.41](https://doi.org/10.1093/mnras/272.1.41)
- Strauss, M. A., Huchra, J. P., Davis, M., et al. 1992, *ApJS*, 83, 29, doi: [10.1086/191730](https://doi.org/10.1086/191730)
- Theios, R. L., Malkan, M. A., & Ross, N. R. 2016, *ApJ*, 822, 45, doi: [10.3847/0004-637X/822/1/45](https://doi.org/10.3847/0004-637X/822/1/45)
- Veilleux, S., Kim, D. C., & Sanders, D. B. 1999a, *ApJ*, 522, 113, doi: [10.1086/307634](https://doi.org/10.1086/307634)
- Veilleux, S., Kim, D. C., Sanders, D. B., Mazzarella, J. M., & Soifer, B. T. 1995, *ApJS*, 98, 171, doi: [10.1086/192158](https://doi.org/10.1086/192158)
- Veilleux, S., Sanders, D. B., & Kim, D. C. 1999b, *ApJ*, 522, 139, doi: [10.1086/307635](https://doi.org/10.1086/307635)
- Veilleux, S., Rupke, D. S. N., Kim, D. C., et al. 2009, *ApJS*, 182, 628, doi: [10.1088/0067-0049/182/2/628](https://doi.org/10.1088/0067-0049/182/2/628)
- Verner, D. A., & Ferland, G. J. 1996, *ApJS*, 103, 467, doi: [10.1086/192284](https://doi.org/10.1086/192284)
- Virtanen, P., Gommers, R., Oliphant, T. E., et al. 2020, *Nature Methods*, 17, 261, doi: [10.1038/s41592-019-0686-2](https://doi.org/10.1038/s41592-019-0686-2)
- Wood, D. O. S., & Churchwell, E. 1989, *ApJS*, 69, 831, doi: [10.1086/191329](https://doi.org/10.1086/191329)
- Yano, K., Nakagawa, T., Isobe, N., & Shirahata, M. 2016, *ApJ*, 833, 272, doi: [10.3847/1538-4357/833/2/272](https://doi.org/10.3847/1538-4357/833/2/272)